

# Dominant clones leverage developmental epigenomic states to drive ependymoma

<https://doi.org/10.1038/s41586-026-10270-8>

Received: 9 August 2024

Accepted: 11 February 2026

Published online: 25 March 2026

Open access

 Check for updates

Alisha S. Kardian<sup>1,2,3,24</sup>, Hua Sun<sup>1,2,24</sup>, Siri Ippagunta<sup>1,2</sup>, Nicholas Laboe<sup>1,2</sup>, Srinidhi Varadharajan<sup>1,2</sup>, Kwanha Yu<sup>4,5</sup>, Hsiao-Chi Chen<sup>4,5</sup>, Erik Emanus<sup>1,2</sup>, Tuyu Zheng<sup>1,2</sup>, Riley M. Deneen<sup>4,5</sup>, Jon P. Connelly<sup>6,7</sup>, Yong-Dong Wang<sup>6,7</sup>, Jiangshan Zhan<sup>8,9</sup>, Hengxi Liu<sup>3,9</sup>, Kimberley Lowe<sup>2</sup>, Taylor Bugbee<sup>1,2,10</sup>, Rakesh Pathak<sup>1,2</sup>, Amanda Bland<sup>1,2</sup>, Sanya Mehta<sup>1,2,10</sup>, Sophie Cochiolo<sup>1,2,10</sup>, Amir Arabzade<sup>1,2</sup>, Blake Holcomb<sup>1,2,10</sup>, Kaitlin M. Budd<sup>1,2,10</sup>, Gabriele Kembuan<sup>1,2</sup>, Tristen Wright<sup>1,2</sup>, Emma Caesar<sup>1,2</sup>, Maxwell Park<sup>1,2</sup>, Amelia Hancock<sup>11</sup>, David Gee<sup>11</sup>, Joel Murdoch<sup>11</sup>, Yi Xiao<sup>12</sup>, Samuel K. McBrayer<sup>12</sup>, Thomas E. Merchant<sup>13</sup>, Jun Qi<sup>14</sup>, Adam D. Durbin<sup>15</sup>, Lindsay A. Schwarz<sup>2</sup>, Li Wang<sup>16,17</sup>, Andrew M. Donson<sup>18</sup>, Nicholas K. Foreman<sup>18</sup>, Sameer Agnihotri<sup>19,20</sup>, Alfonso Lavado<sup>7,21</sup>, Suzanne J. Baker<sup>1,2</sup>, David W. Ellison<sup>22</sup>, Hyun Kyoung Lee<sup>3,5,8,9</sup>, Shondra M. Pruett-Miller<sup>6,7</sup>, Kelsey C. Bertrand<sup>23</sup>✉, Benjamin Deneen<sup>3,4,5</sup>✉ & Stephen C. Mack<sup>1,2</sup>✉

*ZFTA-RELA* is the most recurrent genetic alteration seen in paediatric supratentorial ependymoma (EPN) and is sufficient to initiate tumours in mice<sup>1</sup>. Despite its oncogenic potential, *ZFTA-RELA* (ZR) is observed nearly exclusively in childhood EPN, with tumours located distinctly in the supratentorial brain of the central nervous system<sup>1</sup>. We proposed that specific chromatin modules accessible during brain development would render distinct cell lineage programs at direct risk of transformation by ZR. To test this hypothesis, we performed combined single-nucleus assay for transposase-accessible chromatin and RNA (snMultiome) sequencing of the developing mouse forebrain compared with ZR-driven mouse and human EPN. We demonstrated that specific developmental lineage programs present in transient progenitor cells and regulated by PLAG/L family transcription factors were at risk of neoplastic transformation. Binding of this chromatin network by ZR or other PLAG/L family motifs targeting fusion oncoproteins led to persistent chromatin accessibility at oncogenic loci and oncogene expression. Cross-species analysis of mouse and human ZR EPN revealed significant cell type heterogeneity indicating incomplete neurogenic and gliogenic differentiation, with a small percentage of cycling progenitor-like or radial glial-like cells that established a putative tumour cell hierarchy. In vivo lineage tracing studies identified neoplastic clones that aggressively dominated tumour growth and established the entire EPN cellular hierarchy. These findings identify developmental epigenomic states that are critical for fusion-oncoprotein-driven transformation and show how these states continue to shape tumour progression.

Paediatric cancers are characterized by silent genomes and fewer disease-driving mutations than their adult counterparts<sup>2,3</sup>, and aberrant epigenomes have predominant roles in tumour initiation and development of many childhood cancers<sup>4</sup>. Fusion oncoproteins are common drivers of paediatric cancers and often define their own disease subtypes, for instance, EWSR1-FLI1 in Ewing sarcoma<sup>5</sup>, PAX3-FOXO1 in rhabdomyosarcoma<sup>6</sup>, ETV6-NTRK3 in infantile fibrosarcoma<sup>7</sup> and *ZFTA-RELA* (ZR) in ependymoma (EPN)<sup>1</sup>. Although significant research has focused on molecular characterization of these fusion oncoproteins, the mechanism by which they drive transformation in the context of unique childhood developmental programs is incompletely understood. Specifically, how some of these fusion oncoproteins uniquely

intersect and rewire developmental epigenetic states to transform cells remains unclear. To elucidate these mechanisms, we focused on EPN, the third most common paediatric brain tumour, as a disease model<sup>8</sup>. EPNs are aggressive, chemo-resistant paediatric brain tumours that are characterized by ‘quiet’ genomes with few recurrent genetic alterations but exhibit profoundly aberrant epigenomes<sup>1,9</sup>. *ZFTA* gene fusion events (including *ZFTA-RELA*) are observed nearly exclusively in EPNs and occur specifically in the brain cortex, suggesting a direct relationship between ZR transformation and cortical progenitor populations<sup>1</sup>. EPNs have been reported to arise from a type of radial glial cell (RGC) or gliogenic progenitor cell present during embryonic brain development<sup>10–12</sup>. RGCs are multipotent progenitor cells and

can give rise to neurons and glia in two waves of differentiation during embryonic development<sup>13–17</sup>. Although EPN cells express many RGC markers<sup>10,11,18</sup>, the underlying molecular basis that places these and similar cycling progenitor cells at risk of transformation is not understood. In this study, we sought to understand the epigenomic landscapes of developmental cell lineages that render specific cell types vulnerable to transformation by fusion oncoproteins such as ZR. This was accomplished by dual single-nucleus RNA and assay for transposase-accessible chromatin (ATAC) (herein termed snMultiome) sequencing of the developing mouse brain from embryonic day 12.5 (E12.5) to postnatal day 6 (P6), a time of rapid progenitor cell expansion, as well as integrated characterization across mouse and human ZR EPN tumours. We applied in vivo barcoding technology (Tracker-Seq<sup>19</sup>) to interrogate ZR-driven mouse EPN models and determine the dynamics of malignant clonal diversity through characterization of single-nucleus transcriptional programs and labelled lineage barcodes (LBs). Our investigation of the snMultiome landscapes of EPN across development and disease provide valuable insights into the cell lineage epigenomic programs that shape EPN initiation and progression. These findings may have broader ramifications for our understanding of how fusion oncoproteins leverage distinct chromatin modules in specific cell lineage programs to drive tumour development and cellular heterogeneity.

### Embryonic chromatin accessibility and cancer

ZR functions as an oncogenic transcription factor (TF), activating neoplastic gene expression programs<sup>18,20,21</sup>. This led us to propose that ZR would remodel the developing epigenome and patterns of chromatin accessibility to activate oncogene expression. To test this hypothesis, we isolated putative EPN cells of origin, RGCs<sup>11</sup>, from FABP7-eGFP mice and transduced cells with a lentiviral vector expressing ZR or an empty vector control (Fig. 1a and Extended Data Fig. 1a). Across independent replicates, very minimal changes in patterns of chromatin accessibility were observed in ZR-transformed RGCs profiled by ATAC using sequencing (ATAC-seq) (Fig. 1b). This was in sharp contrast to ZR-driven activation of several thousand transcriptional targets and expression of a core 93-gene signature associated with ZR oncogenic activity (Fig. 1c). These findings suggested that patterns of chromatin accessibility are already established in normal neural progenitor programs and subsequently commissioned by binding of the ZR fusion oncoprotein to induce oncogenic activation.

Although previous CUT&RUN experiments have suggested that PLAGL1/2 binding motifs are shared by ZR, the exact binding sequence and preference of the ZR fusion oncoprotein has remained unknown<sup>18</sup>. To understand the DNA sequence binding preferences of ZR, we adapted the cognate site identification (CSI) assay<sup>22</sup> for use with ZR-expressing HEK293T cell lysates. This involved immunoprecipitation of HA-tagged ZR-expressing cell lysates with a library of 1 trillion unique combinations of double-stranded DNA fragments across a stretch of 20 base pairs. DNA fragments bound by HA-tagged ZR were amplified and reincubated with fresh lysate for subsequent rounds of immunoprecipitation. All rounds (three in total) were then barcoded and pooled for Illumina short-read sequencing. CSI profiling of ZR showed a very strong binding preference for PLAG/L family TF motifs engaged in a dimerized fashion and enrichment of a core GGGCC consensus binding sequence (Fig. 1d,e and Extended Data Fig. 1b). We therefore investigated the accessibility of PLAG/L family TF motifs during embryonic brain development across different developmental cell lineages.

To this end, we microdissected forebrains from mouse embryos at E12.5, E14.5, E16.5, E18.5, P0, P1 and P6, which contained transient progenitor cells, including RGCs<sup>23,24</sup>. Tissues were dissociated and subjected to single-nucleus ATAC-seq (snATAC-seq) and single-nucleus

RNA sequencing (snRNA-seq), using the snMultiome assay developed by 10x Genomics (Fig. 1f). Cell types were annotated using marker sets curated from numerous published studies of the developmental mouse brain (Methods); this identified RGCs, cycling progenitor cells, neurons, astrocytes, oligodendrocyte progenitor cells (OPCs), microglia and endothelial cells, along with their transcriptomic and epigenomic signatures (Fig. 1g,h, Extended Data Fig. 1c,d and Supplementary Table 2). As expected, RGCs were actively proliferating in the early stages, giving rise to postmitotic inhibitory and excitatory neurons (Fig. 1i and Extended Data Fig. 1e–g). Critically, we found that PLAG/L family TF motifs were preferentially accessible in cycling progenitor cells, including RGCs, and chromatin accessibility was reduced upon neuronal differentiation (Fig. 1j,k and Extended Data Fig. 1h–m). These findings were consistent with observations in the developing human fetal brain<sup>25</sup>, with increased PLAGL2 TF activity in RGCs and intermediate progenitor cells that decreased upon differentiation (Fig. 1l). Examination of ZR-specific DNA binding sites in the PLAG/L TF motif data revealed cell-type-specific accessibility in RGCs versus neurons, including at known target genes such as *Gli2*, *Jag1*, *Rela* and *Notch1* (refs. 18,21; Fig. 1m,n and Extended Data Fig. 1n). Finally, to investigate the oncogenic role of PLAG/L TF proteins, we overexpressed *Plagl1*, *Plagl1* and *Plagl2* separately in mouse RGCs and compared transcriptional changes relative to ZR-expressing cells. Overexpression of the PLAG/L TFs did not lead to oncogenic ZR activation, as measured by a failure to recapitulate the 93-gene signature seen in ZR EPN (Extended Data Fig. 2a,b). Similarly, CRISPR-Cas9 knockout of *Plagl1* in both a natively forming and a ZR implant model did not lead to increased survival<sup>11,11,18,21</sup> (Extended Data Fig. 2c–e). Together, these findings pinpoint specific chromatin modules at risk of transformation in specific cell lineages and temporal windows present during brain development as an underlying basis for ZR-driven initiation of EPN.

### Development restrains tumorigenesis

To study the intersection of developmental and ZR-driven oncogenic programs in EPN, we leveraged a natively forming ZR EPN mouse model established by an electroporation-based gene transfer technique called in utero electroporation (IUE) and characterized tumours using snMultiome profiling<sup>26,27</sup>. This involved stable integration of DNA transgenes expressing ZR using the PiggyBac transposon system at E16.5, predominantly targeting RGCs of the lateral ventricles with a PiggyBac transposase (PBase) vector driven by a *Glast* promoter<sup>18</sup>. Cells surrounding the lateral ventricles also express *Plagl1* and known ZR target genes including *Notch1* (Fig. 2a and Extended Data Fig. 2f,g). As controls, we generated a series of YAP1-MAMLD1 (YM)-driven EPN and glioblastoma (GBM) mouse tumours for comparative analyses (Fig. 2b,c). GBMs were established by simultaneous CRISPR-Cas9-mediated knockout of *Nf1*; *Pten*; *Trp53* at E16.5 (Fig. 2b,c; denoted 3xCR). All tumour cell types had unique transcriptional programs, and application of known gene signatures (Supplementary Table 3) could robustly identify tumour cells that corroborated annotations using copy number variant (CNV) analysis (Fig. 2d and Extended Data Fig. 3).

The developmental mouse brain atlas used to identify cell types in normal development (Fig. 1) was then applied to snMultiome profiles of EPN and GBM mouse tumours. We observed diverse patterns of tumour and non-tumour cell types among ZR EPN, YM EPN and 3xCr GBM. Whereas YM EPN was almost exclusively composed of cells with signatures similar to those of RGCs (denoted RGC-like cells), suggesting a complete differentiation ‘block’<sup>28</sup>, ZR EPN tumours showed a diversity of tumour cells with signatures of RGC-like, cycling progenitor-like and neuronal-like cells (Fig. 2e,f and Extended Data Fig. 4). Notably, very few cells along the oligodendrocyte lineage were associated with neoplastic transformation in ZR EPN, in contrast to mouse GBM tumours,

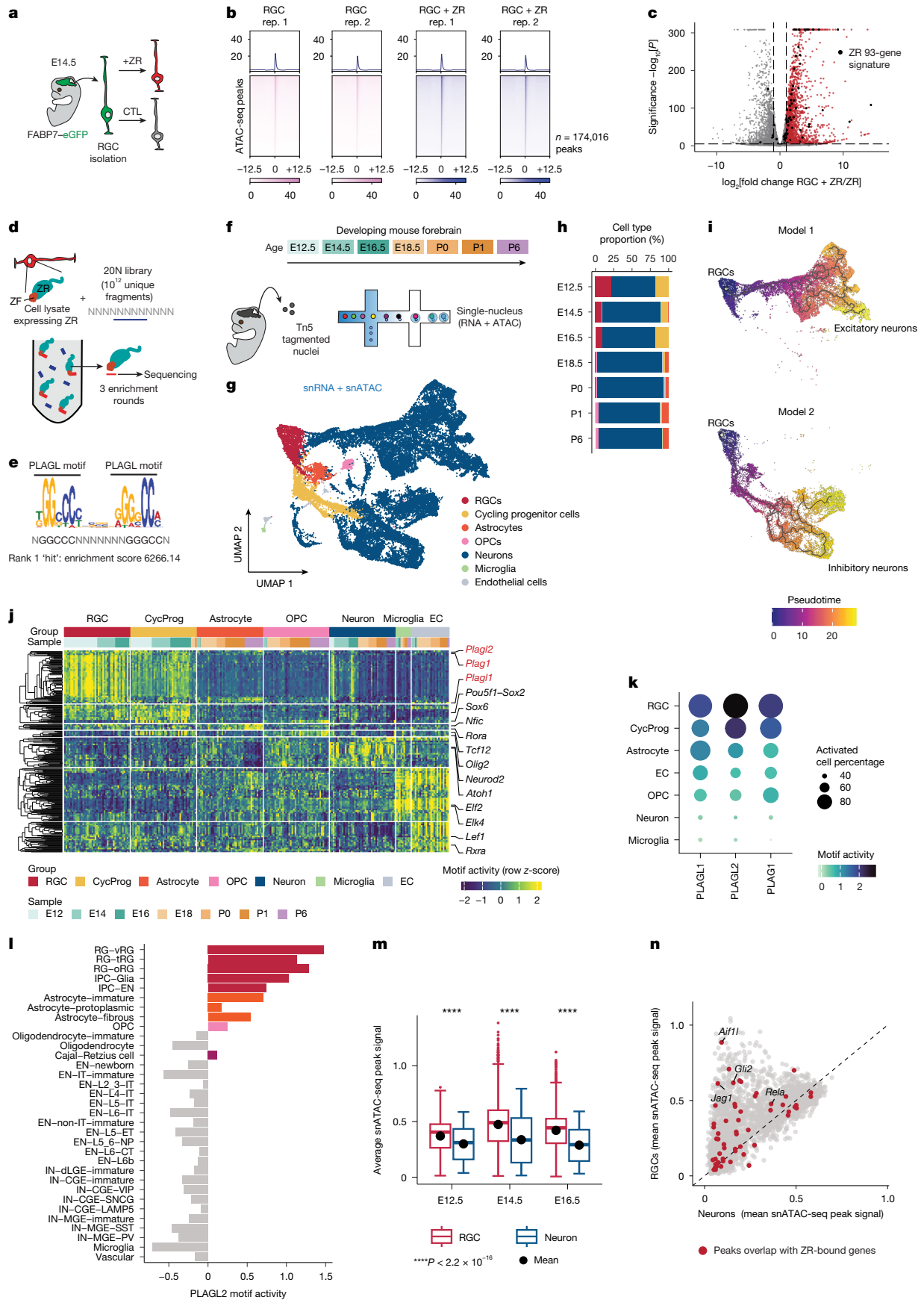


**Fig. 1** | See next page for caption.

### Fig. 1 | Fusion oncoproteins hijack lineage-restricted chromatin accessibility programs at risk of transformation during brain development.

**a**, Schematic illustrating the experimental workflow for generating bulk RNA-seq and ATAC-seq data from control (CTL) and ZR-transformed RGCs. **b**, Genome-wide changes in chromatin accessibility between control RGCs and ZR-transformed RGCs based on ATAC-seq, shown across two technical replicates (rep. 1 and rep. 2). **c**, Volcano plot showing differential gene expression from RNA-seq analysis between control and ZR-transformed RGCs; known ZR signature genes are highlighted. **d**, Schematic illustrating the CSI method for analysis of the binding affinity of ZR for PLAG family motifs. **e**, CSI rank 1 sequence showing the GC-rich PLAG family binding motif. **f**, Schematic depicting the methodology for generating snMultiome data from E12.5 to P6 mouse forebrain. **g**, Uniform manifold approximation and projection (UMAP) plot illustrating the distribution of annotated cell types following integration of the snMultiome data. **h**, Proportions of cell types identified in each of seven normal mouse forebrain samples. **i**, Results of pseudotime analysis showing lineage trajectories from RGCs to excitatory and inhibitory neurons. **j**, Landscape of cell-type-specific motif activation. CycProg, cycling progenitor

cell; EC, endothelial cell. **k**, PLAG family motif activation scores across cell types. Dot size represents the percentage of activated cells. **l**, PLAGL2 motif scores across human developing brain cell types, derived from data published in ref. 25. CGE, caudal ganglionic eminence; CT, corticothalamic; dLGE, dorsal lateral ganglionic eminence; EN, excitatory neuron; ET, extratelencephalic; IPC, intermediate progenitor cell; IT, intratelencephalic; MGE, medial ganglionic eminence; NP, near-projecting; oRG, outer radial glia; PV, parvalbumin; SNCG, synuclein-gamma; SST, somatostatin; tRG, truncated radial glia; VIP, vasoactive intestinal peptide; vRG, ventral radial glia. **m**, Average snATAC peak signal at known ZR binding sites in RGCs and neurons across embryonic stages E12.5, E14.5 and E16.5 in mouse forebrain development. The box plot shows the median (centre line), interquartile range (box) and range (whiskers). Statistical significance between groups at each time point was assessed using a two-sided Wilcoxon rank-sum test without adjustment for multiple comparisons ( $****P < 2.2 \times 10^{-16}$ ). **n**, Scatter plot illustrating average snATAC peak signals in RGCs and neurons at overlapping ZR binding sites, with ZR-associated gene sites highlighted in red.

which demonstrated cellular expansion of the OPC compartment<sup>29,30</sup> (Fig. 2e,f).

To further investigate the potential role of OPC epigenetic states in ZR EPN initiation, we isolated progenitor cells from E14.5 mouse brains, differentiated them to OPCs, and transduced them with a ZR-expressing lentivirus (Extended Data Fig. 5a–c). Unlike in RGCs, ZR expression in OPCs could not activate the full extent of oncogenic targets and did not result in global changes in patterns of chromatin accessibility according to ATAC-seq (Extended Data Fig. 5d,e). To understand whether ZR was still able to initiate tumours in the oligodendrocyte lineage, we performed IUE using two complementary methods: one in which the oligodendrocyte lineage was transformed with ZR at the time of surgery using an *MBP* promoter driving PBase; and one in which all electroporated cells were transformed with an *MBP* promoter driving ZR. In these ZR transformation experiments using these two methods, the oligodendrocyte lineage was either unable to form tumours or formed tumours at a significantly later time point, respectively (Extended Data Fig. 5f–h). Given that human ZR EPNs very rarely express OPC markers (for instance, *OLIG2* and *MBP*)<sup>31</sup>, these data suggest that ZR may engage accessible PLAG/L TF motifs at an earlier time point in development, preceding the emergence of the OPC lineage.

In addition to gene expression differences, tumour types showed unique patterns of TF motif activity consistent with their underlying genetic drivers, including enrichment of PLAG/L TF motifs in ZR EPN, TEAD TF motifs in YM EPN<sup>32</sup>, and IRF TF motifs in GBM<sup>33</sup> (Fig. 2g). Application of the 93-gene signature to mouse ZR EPN revealed widespread ZR target activity across all tumour cell states detected among RGC-like, cycling progenitor-like and neuronal-like cells (Fig. 2d). PLAG/L TF motif activity was detected across all tumour cell types and was highly correlated with ZR target activity (Fig. 2d,h,i and Extended Data Fig. 6a). This was in sharp contrast to normal mouse forebrain development, in which PLAG/L and TEAD TF motif activity decreased upon differentiation (Fig. 1j,k and Extended Data Fig. 6b).

Finally, we quantified the cell cycling state across different cell types identified in ZR-driven EPN mouse tumours (Fig. 2j). This showed that only a subpopulation of cycling progenitor cells and RGCs were actively dividing, with other cell types being mostly non-proliferative. Notably, only cycling progenitors with low-to-moderate ZR activity exhibited the highest cell proliferation signal (Fig. 2j); this was in contrast to other developmental cell types (for instance, neuronal-like), for which far fewer cells were in a proliferative state despite the presence of ZR oncogenic activity. Together, these data demonstrate that the transcriptional diversity of ZR EPN mirrors normal (albeit incomplete) developmental programs and that differentiated cell types are resistant to ZR-induced proliferation, potentially because of their more restricted epigenomic states.

### Convergent epigenomic programs in brain cancer

We sought to corroborate our findings in mouse ZR EPN by studying human EPN samples. Primary tumours from 21 patient samples, comprising 6 ZR-driven EPNs, 10 posterior fossa EPNs (PF-EPNs) and 5 PLAG/L fusion-driven tumours were profiled by snMultiome sequencing (Fig. 3a,b). Upon cell type annotation, the non-tumour cells were found to include endothelial cells, immune cells and oligodendrocytes (Fig. 3b). Malignant and non-malignant cells were defined on the basis of the CNVs detected per cell (Fig. 3c, Extended Data Fig. 7 and Methods). In addition, *t*-distributed stochastic neighbour embedding (*t*-SNE) profiling of snRNA-seq data segregated PF-EPNs and resolved two groups of ZR and PLAG/L fusion-driven tumours (Fig. 3d). Consistent with mouse ZR EPN, we found that ZR fusion activity per cell could be predicted across species using a common 93-gene signature that could robustly stratify ZR-driven EPN tumours (Fig. 3e). There were significant differences in the gene expression signatures of PF-EPNs and those driven by *ZFTA-RELA* or *PLAG/PLAGL* gene fusions ( $n = 465$  genes, adjusted  $P < 0.001$  and average  $\log_2[\text{fold change}] > 1$ ). Notably, at least 20 TF genes showed significantly different expression among the three groups; these included *PAX3* and *MECOM* in PF-EPN, *LHX2* and *RELA* in ZR EPN, and *PAX2* and *SALL3* in PLAG/L fusion-driven tumours (Fig. 3f and Supplementary Table 4).

We next evaluated whether ZR and PLAG/L fused tumours converged upon shared chromatin accessibility programs enriched in developmental PLAG/L TF motifs. As expected, PLAG/L family (*PLAG1*, *PLAGL1*, *PLAGL2*) motifs were highly enriched in the ZR group among the top 100 differential snATAC peaks (Fig. 3g and Supplementary Table 4). PLAGL1/2 motifs were also highly enriched among the top DNA motifs in PLAG/L fused tumours, compared with PF-EPN (Fig. 3h). These data suggest a convergence upon PLAG/L family TF motifs in ZR and PLAG/L fusion-driven tumours. Direct comparison of snATAC results between ZR and PLAG/L showed many shared genomic sites (Fig. 3i), suggesting convergent oncogenic mechanisms. However, highly expressed signature genes of ZR EPN, including *LICAM*, *CCND1* and *WNT3A*, were accessible specifically in ZR EPN, indicating molecular differences (Fig. 3i and Supplementary Table 4). These findings underscore the utilization and diversity of PLAG/L TF family motifs that are leveraged by paediatric fusion oncoproteins to drive brain tumour development.

### Tumour cell diversity mirrors development

We next characterized the cell types present in ZR and PF-EPN and their patterns of chromatin accessibility. Malignant cell types were distinguished based on gene expression markers curated from several published single-cell RNA sequencing (scRNA-seq) studies of human

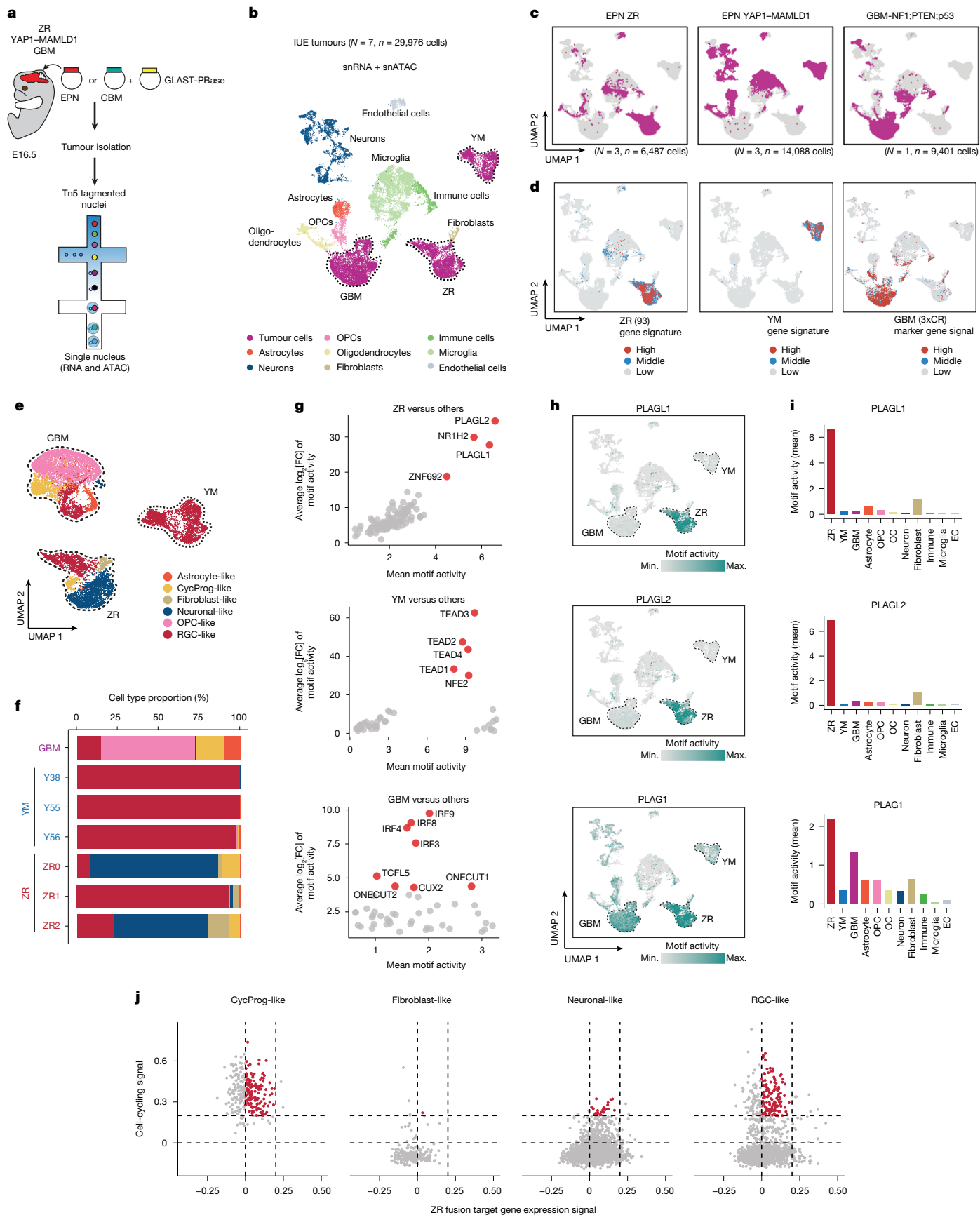


**Fig. 2** | See next page for caption.

**Fig. 2 | Significant enrichment of PLAGL family motif activity in ZR fusion tumour cells.** **a**, Workflow for mouse IUE tumour generation and preparation of snMultiome libraries and data. **b**, UMAP based on weighted nearest-neighbour analysis of integrated snMultiome data from mouse IUE tumours. EPN ZR ( $N = 3$ ), GBM ( $N = 1$ ) and EPN YM ( $N = 3$ ) tumours generated by IUE. Tumour cells were identified by expression of established tumour marker genes. **c**, Cells from each tumour type projected on to integrated UMAP. **d**, Distribution of cells exhibiting tumour gene signatures specific to tumour type. **e**, Reconstructed UMAP based on tumour cells and annotated tumour cell types. **f**, Distribution of tumour cell types across individual tumour samples.

brain development (Methods). Similar to the findings in mouse ZR EPN, snMultiome sequencing identified malignant cells classified as RGC-like, cycling progenitor-like, neuronal-like, fibroblast-like, ependymal-like and astrocyte-like (Fig. 4a–d and Supplementary Table 5). Notably, ependymal-like cells were observed only in human ZR tumours and were absent from mouse ZR tumours (Figs. 4a–d and 2e,f). PF-EPN was largely composed of the same cell types, although in different proportions (Fig. 4a–d, Extended Data Fig. 8a,b and Supplementary Table 5). Given the overrepresentation of PLAG/L TF family motifs in ZR EPN (Fig. 3g–i), we next investigated the enrichment of these DNA motifs within ZR EPN cell populations. We found that PLAG/L motif activity was most elevated in cycling progenitor-like and RGC-like cells and maintained in differentiated cell types such as astrocyte-like and neuronal-like cells (Fig. 4e–g). ZR signatures were also positively correlated with PLAG/L TF motif activity (Fig. 4h,i and Extended Data Fig. 8c,d). Compared with normal cortical development (Fig. 1k,l), this suggests that ZR expression maintains chromatin accessibility of PLAG/L family motifs that are normally repressed during neuronal and glial differentiation. Finally, we predicted cell cycling signatures and compared them with ZR signatures in different malignant cell types. Only cycling progenitor-like cells with low-to-moderate ZR activity exhibited the highest cell proliferation signal, highly consistent with our findings in mouse ZR EPN (Figs. 2j and 4j). Together, these data suggest that in both mouse and human EPN development, ZR abnormally sustains the activity of epigenomic programs—specifically, the PLAG/L cistrome—beyond the normal developmental window, which typically closes upon neuronal cell differentiation.

### Dominant clones establish tumour heterogeneity

To study how developmental lineage programs intersect with tumour heterogeneity, we leveraged an *in vivo* barcoding system called TrackerSeq to label cells and identify barcodes using scRNA-seq<sup>19</sup>. TrackerSeq was used to barcode the developing embryonic brain at the time of EPN initiation. This was achieved by simultaneous incorporation of PiggyBac plasmids expressing ZR and transcribed RNA barcodes using IUE. Following detection by magnetic resonance imaging, tumours were dissected and sorted for positive GFP expression, which labelled successfully TrackerSeq-barcoded cells (Fig. 5a, Extended Data Fig. 9a,b and Supplementary Table 6). Our ZR EPN barcoded cohort consisted of 6 independent experiments with inclusion of multiple replicates totalling  $N = 11$  TrackerSeq datasets. Significant tumour clonal diversity was observed in the early-stage neoplastic lesion, with four- to six-fold greater numbers of LBs detected compared with end-point tumours. However, in most cases, we observed the emergence of a largely single dominant tumour cell clone detected in end-stage tumours (Fig. 5b and Extended Data Fig. 9c–m). In TrackerSeq experiments, tumour cells were identified using a 93-ZR-gene signature (Fig. 5c,d), and dominant LBs (LB-1) were evenly distributed among tumour cells (Fig. 5e). Cell type annotations combined with trajectory analysis showed that dominant tumour cell clones encompassed the entire developmental and transcriptional diversity of mouse ZR EPN (Fig. 5f and Supplementary Table 6), revealing glial and neuronal cell lineage programs emerging from cycling progenitor-like cells.

**g**, Scatter plot illustrating tumour-type-specific motif differences relative to other tumour types. The *x* axis denotes the mean motif score, and the *y* axis represents the average log<sub>2</sub> fold change (FC) in motif activity. Highly differential motifs are highlighted in red and labelled. **h**, Activity states of PLAG family motifs across all cell types, with tumour cell groups indicated. Max., maximum; min., minimum. **i**, PLAG family motif activity across cell types in tumour (ZR, YM, GBM) and non-tumour cell groups. OC, oligodendrocyte cell. **j**, Comparison of cell cycling signal score (*y* axis) with ZR fusion target gene expression signal score (*x* axis) across the various tumour cell types.

In addition, the dominant lineage largely comprised neuronal-like cells (Fig. 5g). These findings identify dominant tumour clones in mouse ZR EPN that drive tumour formation and potentially establish the entire cellular diversity of the disease.

To characterize the cell heterogeneity and potential hierarchy governed by progenitor-like cells in human ZR EPN, we divided tumour cells from ZR EPN according to cycling progenitor or RGC-like signatures and compared them against differentiated programs known to arise from these transient progenitor cells in development, such as neurons, astrocytes and ependymal cells (Extended Data Fig. 10). A gradient of transcriptional states was observed, with cycling progenitor-like and RGC-like cell populations potentially giving rise to less frequently dividing cell types along the glial and neuronal lineages. To understand malignant cell lineage trajectories and determine which cell types develop in early versus late stages of differentiation, we performed pseudotime trajectory inference<sup>34,35</sup> analysis of human ZR EPN; this showed that RGC-like and cycling progenitor-like cells arise ‘early’, followed by the emergence of differentiated neuronal-like, astrocyte-like and ependymal-like cells at later stages (Fig. 5h). Similarly, pseudotime trajectory inference analysis of tumour cells harbouring the dominant LB (LB-1) in TrackerSeq experiments suggested a model in which cycling progenitor-like cells could give rise to astrocyte-like and neuronal-like cells, mirroring normal (albeit incomplete) differentiation programs of the developing cortical brain (Fig. 5i). Together, these data support a model in which EPN cellular heterogeneity is established by dominant progenitor-like cells that give rise to postmitotic or infrequently dividing cells along the glial or neuronal lineages (Fig. 5j).

### Discussion

Paediatric brain cancers are often considered a disease of development<sup>36</sup>, characterized by neoplastic transformation of early developmental cells. In EPN, multipotent RGCs have been proposed to be the candidate cells of origin<sup>10,11</sup>. However, the underlying mechanistic basis for this connection has remained unclear. snMultiome (ATAC + RNA) sequencing characterization of the developing mouse brain revealed a specific chromatin accessibility program in transient cycling progenitor cells (including RGCs) enriched in PLAG/L family TF motifs at direct risk of cellular transformation. ZR fusions, which are observed near-exclusively in EPN<sup>1,11,18,21</sup>, cannot significantly remodel chromatin accessibility but instead engage the already accessible PLAG/L epigenetic program for tumour progression. This led us to consider whether other paediatric cancer drivers (for instance, *PAX3-FOXO1* and *EWS-FLI1*) arise not only in specific cell lineages but engage specific epigenomic programs active during distinct developmental windows that may be primed for cellular transformation.

PLAG/L family proteins have important roles in corticogenesis, patterning, proliferation and development<sup>37–39</sup> and are overexpressed or form fusions in cancer<sup>40–42</sup>. However, they become downregulated and their binding sites correspondingly diminish shortly after birth. Considering the role of PLAGL1 and PLAGL2 in brain development and disease, the ability of ZR to maintain the accessibility of the PLAG/L motif beyond the embryonic stage, in contrast to its regulation during normal development, may be an important mechanism in

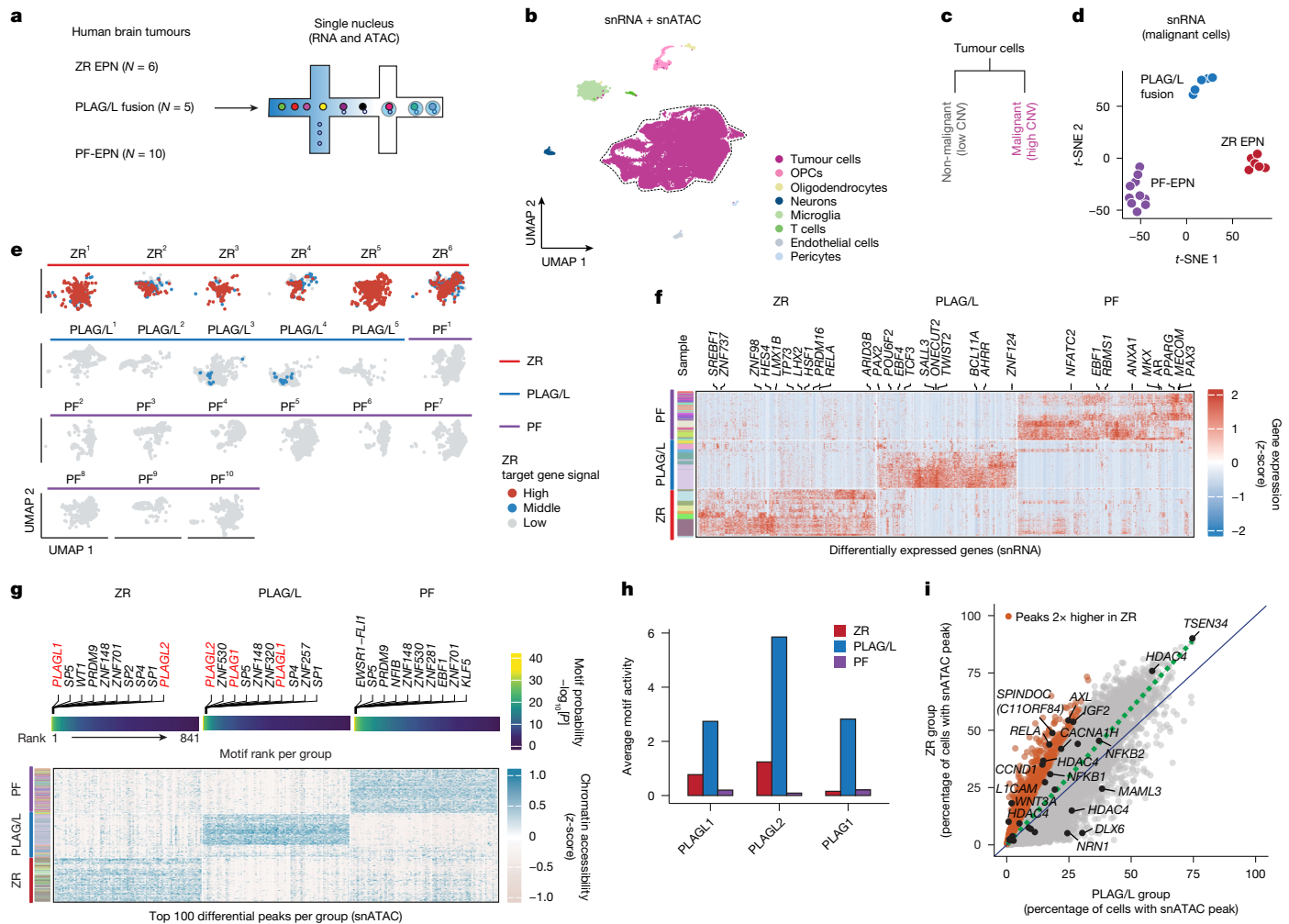


**Fig. 3 | PLAGL family motifs are highly enriched in human ZREPN compared with PF-EPN.** **a**, Schematic of human snMultiome data generation from 21 patients, including ZR fusion-driven EPN ( $N = 6$ ), PLAGL/L fusion-driven tumours ( $N = 5$ ) and PF-EPN ( $N = 10$ ). **b**, Integrated snMultiome data from 21 patients with initial cell type annotation. UMAP was generated by joint analysis of snRNA and snATAC data using the weighted nearest-neighbour method. **c**, Tumour cells were categorized into non-malignant and malignant types according to their degree of CNV. **d**, Analysis of malignant tumour cells using tumour-specific gene expression markers classified patients into three molecular groups (PF-EPN, PLAGL/L fusion and ZR EPN). Specific group characteristics were further validated by DNA methylation analysis. **e**, The ZR target gene signal in malignant cells was assessed across samples by expression of the 93-gene signature. **f**, Heatmap showing genes with significant differential expression among

malignant cells predicted in the three tumour groups. TF-encoding genes with significant expression differences are highlighted. **g**, Heatmap displaying the top 100 differential snATAC peaks identified for each group. Motif enrichment was predicted separately for each group on the basis of the top 100 peaks, with the top 10 enriched motifs highlighted alongside the associated gene names. PLAGL family motifs are highlighted in red. **h**, PLAGL family motif activity in each tumour type. **i**, Comparison of the proportion of cells exhibiting open chromatin at the ZR binding region between the ZR and PLAGL/L groups. Orange dots indicate regions in which the proportion of cells with open ZR binding sites was more than twofold higher in the ZR group compared with the PLAGL/L group. Black-highlighted dots represent ZR fusion target genes. The green dotted line represents the regression line.

EPN initiation. As a result, proliferation genes that promote progenitor cell expansion—such as *Ccnd1*, *Notch1* and *Ephb2*—are probably kept active through terminal glial and neuronal differentiation. In addition to binding of PLAGL/L motifs, the acquisition of strong transcriptional activation domains through gene fusion is likely to play a critical part. In the case of ZFTA fusion oncoproteins, acquisition of intrinsically disordered regions that drive transcriptional condensate formation seems to be necessary for oncogenic transcription and tumour initiation<sup>43</sup>. PLAGL/L fusions may have oncogenic mechanisms that converge with the acquisition of intrinsically disordered regions in *EWSR1* that are critical for gene activation<sup>40,41</sup>.

Our findings may broadly implicate PLAGL/L family DNA motifs as direct targets in brain tumour transformation. In support of this concept, we found shared chromatin accessibility programs that converged on PLAGL/L family TF motifs when comparing ZR EPN with

PLAGL/L fusion-driven brain tumours, which often share EPN-associated histological features<sup>40,41</sup>. Beyond ZR and PLAGL/L, *PLAG1* is amplified and overexpressed in subsets of central nervous system embryonal tumours and is among the top upregulated genes in oncohistone H3 K27M-driven tumours<sup>42,44–46</sup>. These observations led us to propose that the PLAGL/L TF network and its engagement by specific oncoproteins may have broader significance in the development of a wide variety of central nervous system malignancies.

Our study evaluated the intersection of oncogenic and developmental programs from persistent ZR expression during brain development. snMultiome analysis of the ZR-driven IUE model identified diverse cell types with distinct transcriptional and chromatin accessibility programs. These findings were validated across species by snMultiome profiling of mouse and human ZR EPN. Although we anticipated a ‘block’ in development at the RGC state, we also observed continued

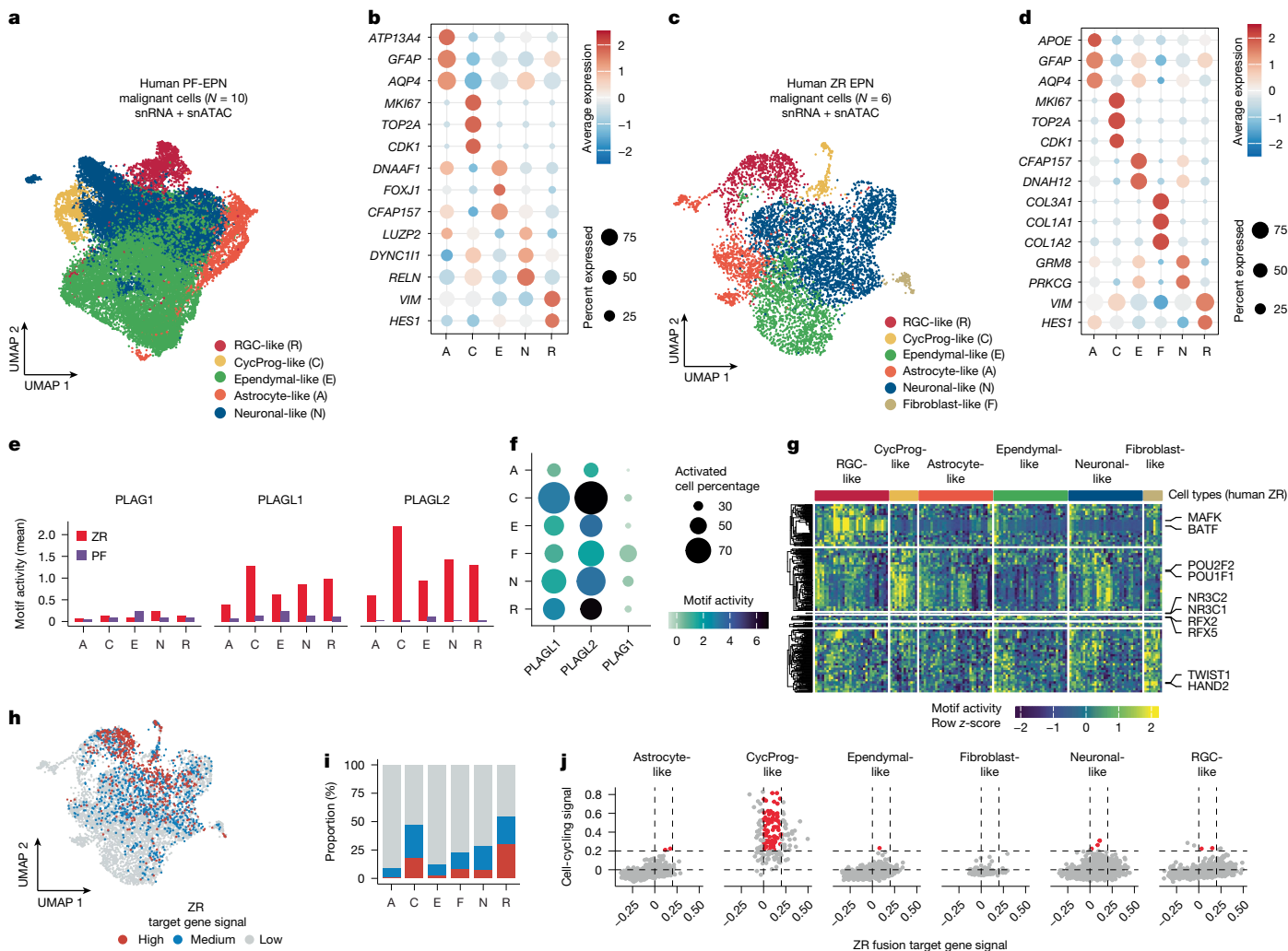


**Fig. 4 | Higher proportion of ZR and PLAGL motif active cells in progenitor cell types.** **a, c.** Annotated cell types among malignant tumour cells from human PF (**a**) and ZR (**c**) snMultiome data. **b, d.** Expression of known marker genes for each malignant tumour cell type in PF (**b**) and ZR (**d**) tumours. **e.** PLAGL family motif activity for each cell type in ZR and PF tumours. **f.** PLAGL1 and PLAGL2 motif activity for each cell type. **g.** Landscape of cell-type-specific

motif activation. **h.** Signal intensity of ZR target genes in malignant cells of ZR tumours, indicated as high (red), medium (blue) and low (grey). **i.** Proportion of cells per cell type with detectable ZR target gene signal. **j.** Comparison of cell cycling signal score (y axis) versus ZR fusion target gene expression score (x axis) across cell types.

(albeit incomplete) differentiation through the glial and neuronal lineages, with most differentiated cells in ZR EPN classified as infrequently cycling or non-cycling. Notably, although this differentiation ‘block’ has not yet been validated in human *YAP1* fusion EPN tumours, it may occur at the RGC stage, consistent with the known role of *YAP1* in regulation of RGC proliferation<sup>47</sup>.

Despite ZR fusion activity across malignant cell types, cell cycle signatures were seen prominently in the progenitor cell state harbouring low-to-moderate levels of ZR target gene expression and rarely in differentiated populations such as neuronal-like and astrocyte-like cells. In normal brain development, RGCs can asymmetrically differentiate to intermediate progenitor cells, which then terminally differentiate to neurons<sup>48–50</sup>. This could suggest a mechanism whereby a minority of transformed ZR-driven cells accumulate in a progenitor state, with most cells continuing to differentiate along the neuronal or glial cell lineages. The elevated number of neuronal-like cells seen in these EPN tumours could suggest an origin in cells already primed to differentiate into neurons, such as RGCs and cycling progenitor cells. A caveat is that the *Glast* promoter used to govern ZR transformation in our experiments is not exclusively active in RGCs and cycling progenitor cells; its activity may be elevated in astrocytes and oligodendrocyte cells.

This limitation is to some extent addressed by the IUE surgery itself, which targets RGCs that line the lateral ventricles at E16.5 of fore-brain development. A further consideration is that the IUE transformation approach decouples endogenous regulation provided by *cis*-regulatory elements surrounding the native oncogene. A potentially more faithful approach would be to genetically engineer the chromosomal rearrangement that leads to *ZFTA-RELA* gene fusion; this may be possible in the future with advances in CRISPR genome-editing technologies.

In vivo lineage tracing (TrackerSeq) experiments of mouse ZR EPN demonstrated the emergence of dominant (often single) clones and the capability of such clones to establish the entire cellular diversity of ZR-driven EPN. Although different molecular barcoding approaches have been previously described in cancer, this has been characterized in only one mouse model of adult glioma (driven by *PDGFB* overexpression) and is distinct from the genetic drivers used to natively model brain tumours such as paediatric EPN<sup>51–53</sup>. Our findings suggest that upon expression of ZR during embryonic brain development, dominant tumour cell clones establish transcriptional diversity, which reflects normal (albeit ‘incomplete’) differentiation programs. This could have important therapeutic applications predicated on induction of cellular

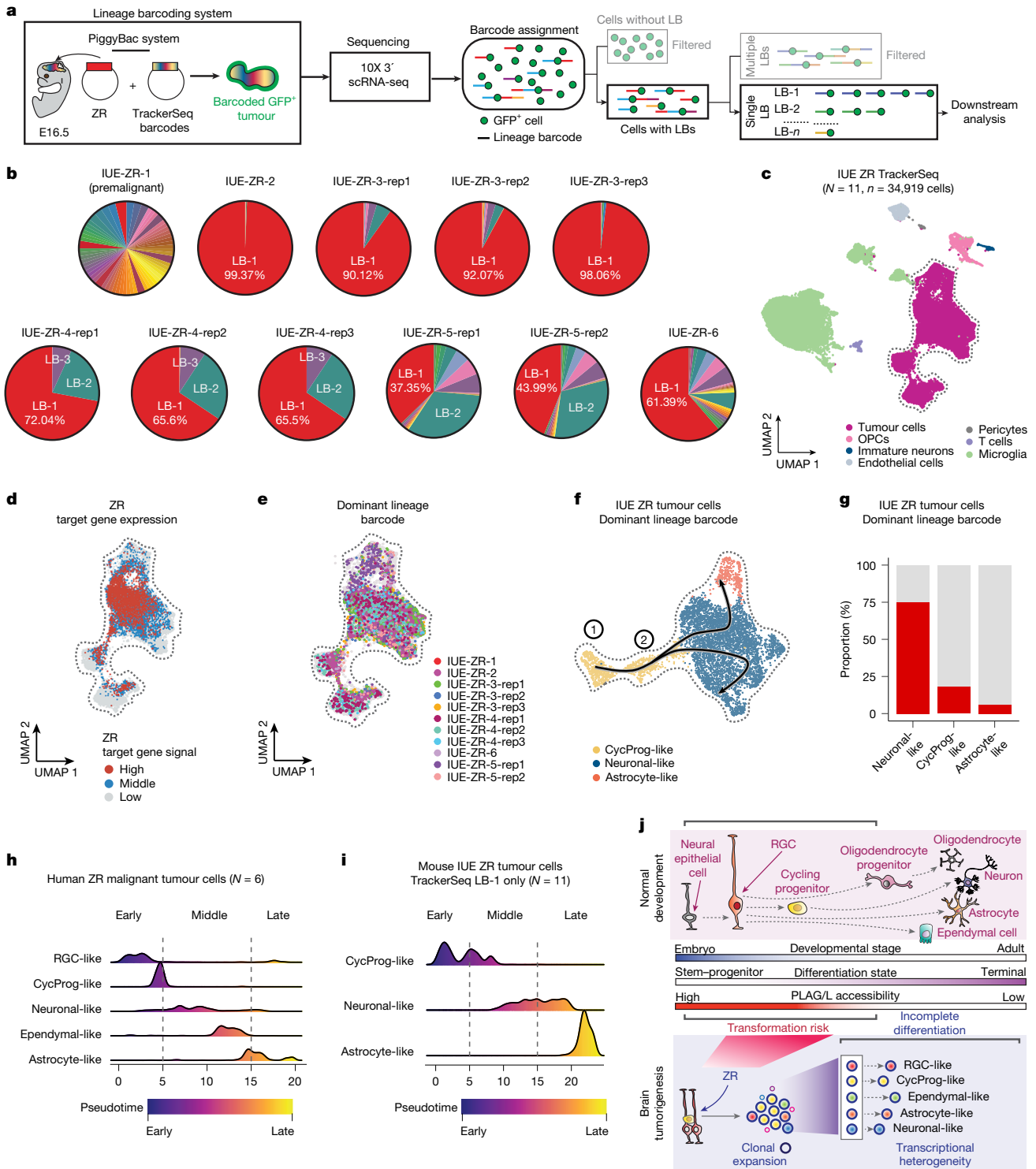


**Fig. 5 | ZR tumour cells harbouring single dominant LBs form independent lineage trajectories.** **a**, Schematic of PiggyBac TrackerSeq lineage barcoding system and raw single-cell RNA data processing workflow. GFP<sup>+</sup> IUE cells were isolated and sequenced, and cells with a single LB were used for downstream analysis. **b**, LB abundance across six IUE biological replicates. Samples IUE-ZR-3 to IUE-ZR-5 included technical replicates. Sample IUE-ZR-1, derived from a P4 mouse brain, showed high diversity in the TrackerSeq library shortly after IUE. **c**, Integrated UMAP of all 11 IUE TrackerSeq datasets, with tumour cell clusters defined by ZR fusion target gene expression enclosed with a dotted line. **d**, UMAP visualization highlighting tumour cell clusters with ZR fusion target gene signal. **e**, Projection of cells harbouring dominant LBs from different samples on to tumour cell clusters in the UMAP, with assessment of barcode

distribution across samples. **f**, UMAP reconstruction performed using tumour cells harbouring dominant LBs. Lineage trajectories were inferred by Slingshot on the basis of Seurat cluster assignments. Arrows denote two distinct differentiation trajectories identified through lineage analysis. **g**, Bar plot illustrating the relative proportions of tumour cell types derived from the dominant LB (LB-1). **h, i**, Pseudotime analysis of human ZR (**h**) and mouse IUE ZR (**i**) tumour cells showing progression from early-stage progenitor-like cells to later-stage differentiated cells. **j**, Schematic summarizing the main findings of our study, showing how shifts in cellular differentiation and progenitor programs correspond with changes in PLAG motif activity, providing insights into molecular mechanisms driving tumorigenesis from neurodevelopmental origins.

differentiation of cycling progenitor-like tumour cells to adopt a more differentiated state that is postmitotic or slowly mitotic, resembling normal development of glial and neuronal cells. The predominance of neuronal-like cells could suggest a lineage-specific differentiation bias, and the interplay between developmental and ZR programs remains to be defined.

Finally, on the basis of mouse and human ZR EPN, we propose a model in which a small proportion of cycling progenitor cells (including RGCs) contribute to EPN initiation and give rise to differentiated cells such as neuronal-like, ependymal-like and astrocyte-like tumour cells. Although our study does not ascribe function to these cells, we have observed hybrid, incompletely differentiated cells in patients with GBM capable of regulating neuronal activity in the tumour micro-environment<sup>54</sup>. Furthermore, we have previously demonstrated in glioma that differentiated malignant cells can contribute to tumour progression by releasing paracrine factors that maintain glioma stem cell identity and regulate tumour progression<sup>55</sup>. Our findings may also explain the highly treatment-resistant nature of EPN, in which persistent and non-dividing or slowly dividing malignant cells resist conventional cytotoxic therapies that target rapidly dividing cell types.

## Online content

Any methods, additional references, Nature Portfolio reporting summaries, source data, extended data, supplementary information, acknowledgements, peer review information; details of author contributions and competing interests; and statements of data and code availability are available at <https://doi.org/10.1038/s41586-026-10270-8>.

1. Parker, M. et al. *C11orf95-RELA* fusions drive oncogenic NF- $\kappa$ B signalling in ependymoma. *Nature* **506**, 451–455 (2014).
2. Sweet-Cordero, E. A. & Biegel, J. A. The genomic landscape of pediatric cancers: Implications for diagnosis and treatment. *Science* **363**, 1170–1175 (2019).
3. Gröbner, S. N. et al. The landscape of genomic alterations across childhood cancers. *Nature* **555**, 321–327 (2018).
4. Panditharatna, E. & Filbin, M. G. The growing role of epigenetics in childhood cancers. *Curr. Opin. Pediatr.* **32**, 67–75 (2020).
5. Grünwald, T. G. P. et al. Ewing sarcoma. *Nat. Rev. Dis. Primers* **4**, 5 (2018).
6. Barr, F. G. et al. Rearrangement of the PAX3 paired box gene in the paediatric solid tumour alveolar rhabdomyosarcoma. *Nat. Genet.* **3**, 113–117 (1993).
7. Davis, J. L. et al. Infantile NTRK-associated mesenchymal tumors. *Pediatr. Dev. Pathol.* **21**, 68–78 (2018).
8. Saleh, A. H. et al. The biology of ependymomas and emerging novel therapies. *Nat. Rev. Cancer* **22**, 208–222 (2022).
9. Mack, S. C. et al. Epigenomic alterations define lethal CIMP-positive ependymomas of infancy. *Nature* **506**, 445–450 (2014).
10. Taylor, M. D. et al. Radial glia cells are candidate stem cells of ependymoma. *Cancer Cell* **8**, 323–325 (2005).
11. Johnson, R. A. et al. Cross-species genomics matches driver mutations and cell compartments to model ependymoma. *Nature* **466**, 632–636 (2010).
12. Vladouiu, M. C. et al. Childhood cerebellar tumours mirror conserved fetal transcriptional programs. *Nature* **572**, 67–73 (2019).
13. Deneen, B. et al. The transcription factor NFIA controls the onset of gliogenesis in the developing spinal cord. *Neuron* **52**, 953–968 (2006).
14. Hirabayashi, Y. et al. Polycomb limits the neurogenic competence of neural precursor cells to promote astrogenic fate transition. *Neuron* **63**, 600–613 (2009).
15. Mission, J. P., Takahashi, T. & Caviness, V. S. Jr. Ontogeny of radial and other astroglial cells in murine cerebral cortex. *Glia* **4**, 138–148 (1991).
16. Noctor, S. C. et al. Neurons derived from radial glial cells establish radial units in neocortex. *Nature* **409**, 714–720 (2001).
17. Noctor, S. C., Martínez-Cerdeño, V. & Kriegstein, A. R. Distinct behaviors of neural stem and progenitor cells underlie cortical neurogenesis. *J. Comp. Neurol.* **508**, 28–44 (2008).
18. Arabzade, A. et al. ZFTA–RELA dictates oncogenic transcriptional programs to drive aggressive supratentorial ependymoma. *Cancer Discov.* **11**, 2200–2215 (2021).
19. Bandler, R. C. et al. Single-cell delineation of lineage and genetic identity in the mouse brain. *Nature* **601**, 404–409 (2022).
20. Kupp, R. et al. ZFTA translocations constitute ependymoma chromatin remodeling and transcription factors. *Cancer Discov.* **11**, 2216–2229 (2021).
21. Zheng, T. et al. Cross-species genomics reveals oncogenic dependencies in ZFTA/C11orf95 fusion-positive supratentorial ependymomas. *Cancer Discov.* **11**, 2230–2247 (2021).
22. Warren, C. L. et al. Defining the sequence-recognition profile of DNA-binding molecules. *Proc. Natl Acad. Sci. USA* **103**, 867–872 (2006).
23. Misson, J. P. et al. Identification of radial glial cells within the developing murine central nervous system: studies based upon a new immunohistochemical marker. *Brain Res. Dev. Brain Res.* **44**, 95–108 (1988).

24. La Manno, G. et al. Molecular architecture of the developing mouse brain. *Nature* **596**, 92–96 (2021).
25. Wang, L. et al. Molecular and cellular dynamics of the developing human neocortex. *Nature* **647**, 169–178 (2025).
26. Saito, T. & Nakatsuji, N. Efficient gene transfer into the embryonic mouse brain using in vivo electroporation. *Dev. Biol.* **240**, 237–246 (2001).
27. John Lin, C. C. et al. Identification of diverse astrocyte populations and their malignant analogs. *Nat. Neurosci.* **20**, 396–405 (2017).
28. Jessa, S. et al. Stalled developmental programs at the root of pediatric brain tumors. *Nat. Genet.* **51**, 1702–1713 (2019).
29. Filbin, M. G. et al. Developmental and oncogenic programs in H3K27M gliomas dissected by single-cell RNA-seq. *Science* **360**, 331–335 (2018).
30. Nagaraja, S. et al. Transcriptional dependencies in diffuse intrinsic pontine glioma. *Cancer Cell* **31**, 635–652 (2017).
31. Otero, J. J., Rowitch, D. & Vandenberg, S. OLIG2 is differentially expressed in pediatric astrocytic and in ependymal neoplasms. *J. Neurooncol.* **104**, 423–38 (2011).
32. Pajtl, K. W. et al. YAP1 subgroup supratentorial ependymoma requires TEAD and nuclear factor I-mediated transcriptional programmes for tumorigenesis. *Nat. Commun.* **10**, 3914 (2019).
33. Lei, J. et al. Interferon regulatory factor transcript levels correlate with clinical outcomes in human glioma. *Aging* **13**, 12086–12098 (2021).
34. Cao, J. et al. The single-cell transcriptional landscape of mammalian organogenesis. *Nature* **566**, 496–502 (2019).
35. Street, K. et al. Slingshot: cell lineage and pseudotime inference for single-cell transcriptomics. *BMC Genomics* **19**, 477 (2018).
36. Filbin, M. & Monje, M. Developmental origins and emerging therapeutic opportunities for childhood cancer. *Nat. Med.* **25**, 367–376 (2019).
37. Adnani, L. et al. *Zac1* regulates the differentiation and migration of neocortical neurons via *Pac1*. *J. Neurosci.* **35**, 13430–47 (2015).
38. Varrault, A. et al. *Zac1* regulates an imprinted gene network critically involved in the control of embryonic growth. *Dev. Cell* **11**, 711–722 (2006).
39. Adnani, L. et al. *Plag1* and *Plagl2* have overlapping and distinct functions in telencephalic development. *Biol. Open* **7**, bio038661 (2018).
40. Sievers, P. et al. Recurrent fusions in *PLAGL1* define a distinct subset of pediatric-type supratentorial neuroepithelial tumors. *Acta Neuropathol.* **142**, 827–839 (2021).
41. Tazuiède-Espariat, A. et al. CNS tumors with *PLAGL1*-fusion: beyond ZFTA and YAP1 in the genetic spectrum of supratentorial ependymomas. *Acta Neuropathol. Commun.* **12**, 55 (2024).
42. Keck, M. K. et al. Amplification of the PLAG-family genes—*PLAGL1* and *PLAGL2*—is a key feature of the novel tumor type CNS embryonal tumor with *PLAGL* amplification. *Acta Neuropathol.* **145**, 49–69 (2023).
43. Arabzade, A. et al. Synthetic ZFTA fusions pinpoint disordered protein domain acquisition as a mechanism of brain tumorigenesis. *Nat. Cell Biol.* **27**, 1496–1509 (2025).
44. Larson, J. D. et al. Histone H3.3 K27M accelerates spontaneous brainstem glioma and drives restricted changes in bivalent gene expression. *Cancer Cell* **35**, 140–155 (2019).
45. Zheng, H. et al. *PLAGL2* regulates Wnt signaling to impede differentiation in neural stem cells and gliomas. *Cancer Cell* **17**, 497–509 (2010).
46. Krug, B. et al. Pervasive H3K27 acetylation leads to ERV expression and a therapeutic vulnerability in H3K27M gliomas. *Cancer Cell* **36**, 338–339 (2019).
47. Cao, X., Pfaff, S. L. & Gage, F. H. YAP regulates neural progenitor cell number via the TEA domain transcription factor. *Genes Dev.* **22**, 3320–34 (2008).
48. Koo, B. et al. Setting the clock of neural progenitor cells during mammalian corticogenesis. *Semin. Cell Dev. Biol.* **142**, 43–53 (2023).
49. Johnson, M. B. et al. Single-cell analysis reveals transcriptional heterogeneity of neural progenitors in human cortex. *Nat. Neurosci.* **18**, 637–46 (2015).
50. Bonnefont, J. & Vanderhaeghen, P. Neuronal fate acquisition and specification: time for a change. *Curr. Opin. Neurobiol.* **66**, 195–204 (2021).
51. Walens, A. et al. Adaptation and selection shape clonal evolution of tumors during residual disease and recurrence. *Nat. Commun.* **11**, 5017 (2020).
52. Ho, I. L. et al. Clonal dominance defines metastatic dissemination in pancreatic cancer. *Sci. Adv.* **10**, eadd9342 (2024).
53. Ceresa, D. et al. Early clonal extinction in glioblastoma progression revealed by genetic barcoding. *Cancer Cell* **41**, 1466–1479 (2023).
54. Curry, R. N. et al. Integrated electrophysiological and genomic profiles of single cells reveal spiking tumor cells in human glioma. *Cancer Cell* **42**, 1713–1728.e6 (2024).
55. Wang, X. et al. Reciprocal signaling between glioblastoma stem cells and differentiated tumor cells promotes malignant progression. *Cell Stem Cell* **22**, 514–528 (2018).

**Publisher's note** Springer Nature remains neutral with regard to jurisdictional claims in published maps and institutional affiliations.



**Open Access** This article is licensed under a Creative Commons Attribution-NonCommercial-NoDerivatives 4.0 International License, which permits any non-commercial use, sharing, distribution and reproduction in any medium or format, as long as you give appropriate credit to the original author(s) and the source, provide a link to the Creative Commons licence, and indicate if you modified the licensed material. You do not have permission under this licence to share adapted material derived from this article or parts of it. The images or other third party material in this article are included in the article's Creative Commons licence, unless indicated otherwise in a credit line to the material. If material is not included in the article's Creative Commons licence and your intended use is not permitted by statutory regulation or exceeds the permitted use, you will need to obtain permission directly from the copyright holder. To view a copy of this licence, visit <http://creativecommons.org/licenses/by-nc-nd/4.0/>.

© The Author(s) 2026

<sup>1</sup>Center of Excellence in Neuro-Oncology Sciences, St Jude Children's Research Hospital, Memphis, TN, USA. <sup>2</sup>Department of Developmental Neurobiology, St Jude Children's Research Hospital, Memphis, TN, USA. <sup>3</sup>Cancer and Cell Biology Program, Baylor College of Medicine, Houston, TX, USA. <sup>4</sup>Cell and Gene Therapy Program, Baylor College of Medicine, Houston, TX, USA. <sup>5</sup>Center for Cancer Neuroscience, Baylor College of Medicine, Houston, TX, USA. <sup>6</sup>Center for Advanced Genome Engineering, St Jude Children's Research Hospital, Memphis, TN, USA. <sup>7</sup>Department of Cell and Molecular Biology, St Jude Children's Research Hospital, Memphis, TN, USA. <sup>8</sup>Department of Pediatrics, Section of Neurology, Baylor College of Medicine, Houston, TX, USA. <sup>9</sup>Jan and Dan Duncan Neurological Research Institute, Texas Children's Hospital, Houston, TX, USA. <sup>10</sup>St Jude Children's Research Hospital Graduate School of Biomedical Sciences, Memphis, TN, USA. <sup>11</sup>University of Bath, Bath, UK. <sup>12</sup>Children's Medical Center Research Institute, UT Southwestern, Dallas, TX, USA. <sup>13</sup>Radiation Oncology Department, St Jude Children's Research Hospital, Memphis, TN, USA. <sup>14</sup>Cancer Biology

Department, Dana-Farber Cancer Institute, Boston, MA, USA. <sup>15</sup>Division of Molecular Oncology, Department of Oncology, St Jude Children's Research Hospital, Memphis, TN, USA. <sup>16</sup>Department of Neurology, University of California San Francisco, San Francisco, CA, USA. <sup>17</sup>The Eli and Edythe Broad Center of Regeneration Medicine and Stem Cell Research, University of California San Francisco, San Francisco, CA, USA. <sup>18</sup>Department of Pediatrics, University of Colorado Anschutz Medical Campus, Aurora, CO, USA. <sup>19</sup>Department of Neurological Surgery, University of Pittsburgh, Pittsburgh, PA, USA. <sup>20</sup>Children's Hospital of Pittsburgh, Pittsburgh, PA, USA. <sup>21</sup>Center for Pediatric Neurological Disease Research, St Jude Children's Research Hospital, Memphis, TN, USA. <sup>22</sup>Department of Pathology, St Jude Children's Research Hospital, Memphis, TN, USA. <sup>23</sup>Department of Oncology, St Jude Children's Research Hospital, Memphis, TN, USA. <sup>24</sup>These authors contributed equally: Alisha S. Kardian, Hua Sun. <sup>✉</sup>e-mail: kelsey.bertrand@stjude.org; deneen@bcm.edu; stephen.mack@stjude.org

## Methods

### In utero electroporation

All animal procedures in this study were performed with approval from the St. Jude Institutional Animal Care and Use Committee. IUE was performed as described previously<sup>27</sup>, and plasmids were prepared with a NucleoBond Xtra Maxi Plus EF kit (Takara Biosciences). After anaesthesia with 4.5% isoflurane, pregnant CD1 mice at E16.5 were subjected to abdominal incision to expose the uterus. A DNA plasmid cocktail (1  $\mu\text{g } \mu\text{l}^{-1}$  pBCAG-HA-ZR<sup>FUS1</sup>, 1  $\mu\text{g } \mu\text{l}^{-1}$  pBCAG-eGFP-Luciferase, 1.5  $\mu\text{g } \mu\text{l}^{-1}$  pX330-sg*Trp53*, 2  $\mu\text{g } \mu\text{l}^{-1}$  GLAST-PBase, 1.5  $\mu\text{g } \mu\text{l}^{-1}$  m*Plagl1* single-guide RNA, 0.5  $\mu\text{g } \mu\text{l}^{-1}$  TrackerSeq library, FastGreen dye) was injected into the lateral ventricles with a glass pipette. Electric pulses were then delivered to the embryos by gently clasping their heads with forceps-shaped electrodes. Six 33-V pulses of 55 ms were applied at 100-ms intervals. The uterus was then repositioned into the abdominal cavity, the abdominal wall was sutured and the skin was stapled. Following birth, pups were monitored for clinical signs of tumour growth (such as seizures, circling, and head doming), as well being monitored by magnetic resonance imaging every 2 weeks. At end point, mice were collected for isolation of nuclei or immunofluorescence staining. In accordance with our St. Jude Institutional Animal Care and Use Committee protocol, end point was defined on the basis of a set of neurological symptoms (gait, hunching, kyphosis, squinting), and these limits were not exceeded in any of the experiments. Mice for isolation of nuclei were perfused with 10 ml cold PBS, and tumours were frozen in isopentane and stored at  $-80^{\circ}\text{C}$ . For survival curves, pups from a minimum of 2 mothers were included. Randomization and blinding were not applicable.

### RGC isolation

RGCs were previously isolated from *Ink4a*-knockout mice with GFP expressed from the *Blbp* promoter using a Worthington Papain Dissociation system (LK003150). Cells were grown in neural basal medium (Invitrogen) supplemented with sodium pyruvate, glutamine, B27, N2, bFGF (10 ng  $\text{ml}^{-1}$ ) and rhEGF (20 ng  $\text{ml}^{-1}$ ) and tested for mycoplasma monthly. Cells were grown on treated cell culture dishes coated with Matrigel (Corning). RGCs were made ZR positive using a lentivirus generated by the Viral Vector Core at St. Jude. Mouse tumour cells were seeded into 10-cm plates 24 h before infection and infected with lentivirus with 8  $\mu\text{g } \text{ml}^{-1}$  polybrene for 24 h. Infected cells were selected with 2  $\mu\text{g } \text{ml}^{-1}$  puromycin for 3 days. ZR expression was confirmed by western blotting. Single-guide RNAs for *Plagl1* were generated by the Center for Advanced Genome Engineering with an Addgene 52961 backbone, which included RFP. ZR-positive RGCs were infected by the same method and sorted for RFP using a BD FACSAria Fusion system. Knock-out of more than 90% was confirmed by targeted deep sequencing.

### OPC isolation

Primary OPC cultures were performed as previously described<sup>56,57</sup>. In brief, cortical tissues from E14.5 mouse embryos were collected, and neural stem cells were cultured as neurospheres for 4 days. Neural stem cells were dissociated and plated on poly-D-lysine-coated dishes at a density of  $1.5 \times 10^4$  cells  $\text{cm}^{-2}$  in OPC media. They were subsequently infected with either ZR-Lenti-Cherry or control virus for 14 h. After viral infection, cells were maintained in OPC medium for 4 days before being collected for ATAC-seq and RNA-seq.

### RNA-seq and ATAC-seq analyses

RNA-seq and ATAC-seq analyses were performed using Genialis Expression software (<https://www.genialis.com>) deployed locally on St. Jude HPC infrastructure. Briefly, the RNA-seq pipeline run on the Genialis platform comprised the following steps. Raw reads were filtered to remove adaptors and poor-quality reads using BBDuk (v.37.9; <https://sourceforge.net/projects/bbmap/>). The resulting reads were mapped

to the reference genomes (Ensembl 92) using STAR (v.2.7.0; RRID SCR\_015899). FeatureCounts (v.1.6.3; RRID SCR\_012919) was used for quantification of gene expression levels, followed by DESeq2 (RRID SCR\_000154) for differential gene expression analysis. Genes with low expression (expression count summed over all samples of less than 10) were filtered out from the input matrix to DESeq2. The paired-end reads from ATAC-seq were trimmed using BBDuk (v.37.9) and mapped to reference genome mm10 using Bowtie2 (v.2.3.4.1). MACS2 (v.2.1.1.20160309) was then used to call peaks on the aligned reads using a *P* value cutoff of 0.01 (parameters  $-\text{shift } -75 -\text{extsize } 150 -\text{nomodel } -\text{call-summits } -\text{nolambda } -\text{keep-dup all } -P = 0.01$ ).

### TrackerSeq library generation and validation

TrackerSeq library cloning was carried out generally as described in ref. 19. In brief, the pCAG-SacB plasmid was digested with BstXI, and the 8-bit barcode was cloned into it using NEBuilder HiFi master mix (six reactions in total), followed by isopropanol purification. Purified reactions were electroporated into Endura DUOs (Lucigen) using a MicroPulser with program Ec1 (Bio-Rad). Four electroporations were carried out then recovered for 1 h at  $37^{\circ}\text{C}$  in 2 ml of recovery media. Next, cells were plated overnight at  $32^{\circ}\text{C}$  on 245-mm plates (Corning). The following morning, plates were scraped and cells were collected in Luria Broth (Miller), and library plasmids were purified using Endofree midprep kits (Qiagen). For validation, 10 ng of the library plasmid prep was amplified using 2xPhusion (NEB) and sequenced by the Hartwell Center for Genome Sequencing Facility at St. Jude.

### CSI DNA binding assay

HEK293T cells were transiently transfected with HA-tagged ZR fusion plasmids using Lipofectamine 2000 reagent according to the protocol (Thermo Fisher 11668019). Following expression, cells were lysed with RIPA buffer (Thermo Fisher 89900) and spun down for collection of supernatant. A DNA library (Integrated DNA Technologies) containing randomized central regions of 20 bp flanked by constant sequences complimentary to primers was converted to double-stranded DNA and brought to 74 ng  $\mu\text{l}^{-1}$  before being combined with 1% w/v bovine serum albumin, 500 ng  $\mu\text{l}^{-1}$  poly dI-DC (Thermo Fisher 20148E), 1% NP-40 (Thermo Fisher 85124), and 10 $\times$  PBS. ZR-positive and ZR-negative cell lysates were incubated with this mixture for 1 h at room temperature. The mixture was then added to anti-HA beads (Thermo Fisher 88836) washed in binding buffer (10 $\times$  PBS, 1% bovine serum albumin, 1% NP-40) and incubated for 30 min. Solutions were washed in binding buffer and aspirated on a magnetic plate three times before being resuspended in a PCR master mix (Lucigen Econo Taq 2 $\times$ 30035-1 and custom primers). Library fragments attached to beads were amplified on a Bio-Rad thermal cycler and then purified using a New England Biolabs Monarch PCR & DNA clean-up kit (T1030L). Eluted DNA library fragments from each sample were diluted to a concentration of 74 ng  $\mu\text{l}^{-1}$  and checked on a gel before being incubated with cell lysates again. Following three rounds of incubation and amplification, all purified library fragments from each round for each sample were given a unique barcode and a sequencing adaptor and then sequenced with a NovaSeq short-read sequencing amplicon kit, yielding approximately 500 million reads. Sequencing results were sorted by barcode, and the 20-bp library regions selected in each sample were ranked by enrichment and normalized to fusion negative lysate samples. Primer sequences were as follows: forward 5'-CTGATCCTACCATCCGTGCT-3', reverse 5'-CCGCTCGGTACGAAGCTG-3'.

### Nuclei isolation

Tissue (10–30 mg) was cut from human tumours and input into a 10 $\times$  Nuclei Isolation Kit (PN-1000494). Kit instructions were followed, but the lysis buffer incubation time was increased to 15 min to isolate quality nuclei. Mouse embryonic forebrain was isolated with the 10 $\times$  Demonstrated Protocol CG000366 RevD, but lysis buffer incubation

was decreased to 2 min. IUE tumours were isolated with a Dounce homogenizer and iodixanol gradient using a modified version of the protocol described in ref. 58. Nuclei were resuspended in nuclei buffer and counted with a haemocytometer, and 10,000 were loaded on to a 10x Chromium Chip. Libraries were assessed with an Agilent TapeStation and sent for sequencing at St. Jude's Hartwell Center on a NovaSeq 6000. Gene expression libraries had 400 million reads with a 28-10-10-90 cycle configuration, and ATAC libraries had 500 million reads with a 50-8-24-49 cycle configuration.

### RNAscope

End-point ZR tumour-bearing mice were cervically dislocated, and brains were removed from the skull. Brains were flash-frozen in isopentane and frozen in OCT blocks, which were kept at  $-80^{\circ}\text{C}$ . Sections were cut on a Leica 3050 cryostat at  $16\ \mu\text{m}$ , and slides were kept at  $-80^{\circ}\text{C}$  until ready for use. The ACDBio Multiplex Fluorescent v.2 fresh frozen RNAscope protocol (revision B UM 323100) was followed with slight modifications: protease III was used for 30 min, opal fluorophores were used at 1:750, and DAPI was used at 1:5,000 for 20 min. The probes used were a custom C1 *Zfta* probe targeting [TGGCGTTGGAGTATCTCATGGATTCAACCCAGCGAGGCACGGCATGTGTGCATGGTCTGCGGTAGCTCTTTGGCTACCCTGAAGCTGAGCAC TATCAAACGCCACATCCGTCAGAAGCACCCGTACAGCCTGCAT], *Cdk1* 476081-C2, *Pax6* 412821-C3, *Eomes* 429641-C3, *Grin1* 431611-C3, *Pdgfra* 480661-C3, *Mog* 492981-C3 and *Kif6* 1760891-C3. Images were taken on a Zeiss LSM 780 at  $\times 20$  using a 9-square tile scan and maximum intensity projection of a z-stack.

### Immunofluorescence

IUE surgery was performed with PBCAG-GFP at  $4\ \mu\text{g}\ \mu\text{l}^{-1}$ . Brains were taken from P2 pups and placed in 4% paraformaldehyde at  $4^{\circ}\text{C}$  with shaking for 24 h. They were then transferred to 30% sucrose until they sank (approximately 48 h). They were frozen in OCT and kept at  $-80^{\circ}\text{C}$  until ready for cutting. Brains were cut at  $16\ \mu\text{m}$  on a Leica 3050 cryostat, and slides were kept at  $-20^{\circ}\text{C}$  until ready for use. Slides were then permeabilized for 20 min (0.3% Triton in PBS), blocked for 1 h (5% normal donkey serum, 0.3% Triton in PBS), incubated with primary antibody overnight (GFP Aves, 1:2,000), incubated in secondary antibody for 1 h at room temperature (Thermo A78948), incubated in 1:5,000 DAPI (Thermo 62248) for 20 min, and mounted with Fluoromount G (Thermo 00-4958-02). For immunofluorescence of primary OPCs, cells were washed three times in PBS, permeabilized in PBST (0.3% Triton/PBS) for 5 min, washed again, blocked with 10% normal goat serum in PBST for 1 h at room temperature, and incubated overnight at  $4^{\circ}\text{C}$  with primary antibodies (Mouse OLIG2, Millipore MABN50, 1:500; Rabbit HA, sc-805, 1:1,000). After washing, cells were incubated with secondary antibodies for 1 h at room temperature, washed, stained with DAPI and mounted in VectaShield Antifade. All images were acquired on a Zeiss LSM 780 confocal microscope at  $\times 20$  using maximum intensity projections of z-stacks.

### snMultiome data processing

For both human and mouse datasets, the 'cellranger-arc count' pipeline (10x Genomics, v.2.0.1, <https://www.10xgenomics.com>) was used for cell barcode detection, read alignment and quality assessment, following the standard 10x Genomics protocols. Human reads were aligned to the GRCh38 reference genome (refdata-cellranger-arc-GRCh38-2020-A-2.0.0, based on GENCODE v.32) and mouse reads to the mm10 reference genome (refdata-cellranger-arc-mm10-2020-A-2.0.0, based on GENCODE v.M23). The pipeline performed initial quality control by distinguishing intact nuclei from background and removing non-nucleus-associated reads. Subsequently, ambient RNA contamination per sample was assessed using SoupX (<https://github.com/constantAmateur/SoupX>) on the prefiltered data. Samples that passed both the initial quality control metrics reported in the Cell Ranger ARC

QC summary and the SoupX contamination thresholds were retained for downstream analysis. We assessed data quality at the individual nucleus level and retained high-quality nuclei using Seurat (v.5.1.0, <https://satijalab.org/seurat>) and Signac (v.1.14.0, <https://github.com/timoast/signac>), applying the following criteria: total ATAC fragment count (nCount\_ATAC) of at least 3,000, transcription start site enrichment scores between 2 and 15, total RNA counts (nCount\_RNA) of at least 2,000, detected gene counts (nFeature\_RNA) ranging from 500 to 8,000, and mitochondrial gene percentages less than 10%. For exclusion of doublets, doublet probabilities were estimated using DoubletFinder (v.2.0.4, <https://github.com/chris-mcginnis-ucsf/DoubletFinder>), and nuclei with high doublet scores were removed. DropletQC<sup>59</sup> was applied to further identify and filter potential empty droplets, ensuring that only high-quality nuclei were retained for downstream analysis.

### snMultiome data integration

For snATAC data of snMultiome analysis, open chromatin region peaks were called on individual samples using MACS2 (v.2.2.7, <https://github.com/macs3-project/MACS>) with the CallPeaks function in Signac (v.1.14.0), with intervals overlapping ENCODE blacklist regions excluded. To integrate all snATAC-seq data, we first created a unified set of peaks for quantification across datasets using the GenomicRanges package, filtering out peaks shorter than 20 bp or longer than 10,000 bp. Fragments for each sample were then recalled on the basis of this unified peak set. Top features in each snATAC-seq dataset were identified using FindTopFeatures (min.cutoff = 10), followed by TF-IDF normalization with the RunTFIDF function and latent semantic indexing (LSI) dimensionality reduction using the RunSVD function in Signac. After merging the datasets, we repeated these steps on the combined data. The snATAC data were then integrated using the FindIntegrationAnchors and IntegrateEmbeddings functions. Finally, nonlinear dimensionality reduction was performed using RunUMAP on LSI components 2 to 40. For snRNA data, normalization and data scaling were performed on the merged snRNA dataset using SCTransform v.2, followed by principal component analysis (PCA) and uniform manifold approximation and projection (UMAP) dimensionality reduction using the RunPCA and RunUMAP function in Seurat (v.5.1.0). Weighted nearest-neighbour analysis was done using Seurat with 1–30 principal components from snRNA data and 2–30 integrated LSI components from snATAC data. The resulting nearest-neighbour graph was then used for UMAP embedding and clustering following the best practice described in Seurat and Signac for multiome data analysis.

### Estimation of motif activity from snATAC-seq data

Motif/TF chromatin accessibility (motif activity) was computed for a set of 841 TFs (combined mouse and human TFs) from the JASPAR 2022 database using the RunChromVAR function in Signac (v.1.14.0), and differential motif activity was computed with the FindMarkers function. Motif enrichment in the differentially accessible regions was analysed with the FindMotif function.

### Cell type annotation for snMultiome and scRNA

Cell type annotation of single-cell data was performed using Cell-TypeEstimate (v.0.3.1; <https://github.com/combiozone/CellTypeEstimate>), an in-house tool adapted from the published tool ScType (<https://github.com/lanevskiAleksandr/sc-type>), incorporating custom code modifications and an alternative reference database. Marker sets were derived from more than 40 published studies of human and mouse brain development. References for each marker set are recorded in the 'source' column of the marker database files (db/\*.xlsx). Following automated annotation, all labels were manually reviewed and refined to ensure biological accuracy. For tumour samples, the suffix '-like' was manually appended to each annotated tumour cell type.

## Processing of TrackerSeq barcode reads

We processed TrackerSeq barcode reads following the methods described in ref. 19 ([https://github.com/mayer-lab/Bandler-et-al\\_lineage](https://github.com/mayer-lab/Bandler-et-al_lineage)). Reads from the R2 FASTQ files were pre-processed by trimming the flanking sequences on both sides of the LBs. Barcodes shorter than 37 bp were discarded. A whitelist of cell barcodes was generated using UMI-tools. These whitelisted cell barcodes, along with their corresponding unique molecular identifiers, were appended to the read names in the LB FASTQ files to produce new, modified FASTQ files. The modified files were then used for downstream processing, including matching of LBs to cells and further filtering of the LBs. To isolate high-confidence LBs, we retained only those containing the conserved nucleotide motif ‘...CTG...ACT...GAC...TGA...CTG...ACT...GAC...’ and excluded any barcodes with ambiguous bases (N). These high-confidence LBs were matched to clean cells from the Seurat object, resulting in a set of cells with confidently assigned LBs. Cells were classified as either single LB, containing one unique LB per cell, or multiple LB, containing more than one LB per cell, on the basis of these assignments. In the single-LB group, LBs were ranked by number of associated cells, with those having the highest counts designated as dominant single LBs (typically referred to as LB-1). Only cells with a single LB were retained for downstream analyses.

## TrackerSeq data analysis from quality control to cell type annotation

Raw TrackerSeq data were processed using Cell Ranger (v.9.0.0, <https://www.10xgenomics.com>) with mm10 (10x Genomics, `refdata-cellranger-mm10-2020-A-2.0.0`) as the reference genome. Then, `filtered_feature_bc_matrix` data were used to filter pooled cells and normalized in Seurat. We selected high-quality cells on the basis of cutoffs such as more than 500 genes, more than 2,000 unique molecular identifiers (`nCount_RNA`), less than 10% of mitochondrial genes, and less than the customized maximum quantile for `nFeature_RNA` (less than  $\text{quantile}(\text{probs} = 0.9)$  and no more than 8,000) and `nCount_RNA` (less than  $\text{quantile}(\text{probs} = 0.99)$ ). Next, we used DoubletFinder (v.2.0.4) to estimate doublets, retaining only cells classified as ‘Singlet’, and removed empty droplets on the basis of DropletQC filtering. Afterwards, data were normalized using the SCTransform v.2 method in Seurat (v.5.1.0), regressing out the percentage of mitochondrial gene expression (`percent.mt`) to reduce its confounding effects. Last, high-quality cells were used to perform PCA, UMAP and clustering analyses in Seurat. Cell type annotation was then carried out using CellTypeEstimate (v.0.3.1) on the basis of the identified clusters. In downstream analyses, this information was integrated with LB-matched cells to enable more in-depth analysis. For the integration analysis, we merged all high-quality cells from independent TrackerSeq datasets using Seurat (v.5.1.0), performed SCTransform v.2 normalization (regressing out mitochondrial percentage) and PCA, applied Harmony (v.1.2.3; <https://github.com/immunogenomics/harmony>) with the `IntegrateLayers` function, and used the top 30 Harmony embeddings for UMAP visualization and clustering.

## Classification of malignant cells

To classify cells as malignant or non-malignant, we inferred genome-wide CNVs using InferCNV (v.1.22.0, <https://github.com/broadinstitute/infercnv>) with default parameters. InferCNV was run at the sample level with integrated count matrices of snRNA-seq and snATAC-seq data, separately. The reference used immune cells and microglial cells. We first defined the CNVs as loss (InferCNV value  $\leq 0.8$ ) or gain (InferCNV value  $\geq 1.2$ ) and filtered CNV regions (hidden Markov model outputs) with fewer than 20 genes to detect large-region ( $\geq 5$  Mb) chromosomal CNVs. Next, we calculated the copy number alteration ratio per CNV

region. Last, we estimated malignant cells as those with large CNV regions (at least 100 CNV genes in the region) or a CNV ratio greater than 0.5 per sample.

## ZR fusion signal signatures

The single-cell ZR fusion signature was calculated on the basis of 93 ZR driver genes<sup>18,20,45</sup> using the `AddModuleScore` function in Seurat (v.5.1.0). We considered a score on our in-house benchmark test greater than 0.2 to indicate confidence, whereas scores of 0.1–0.2 indicated uncertainty, and scores less than 0.1 indicated distrust. Scores greater than 0.1 corresponded to the ZR target gene signal, whereas scores less than 0.1 indicated non-signal.

## Cell cycling and non-cycling signatures

The `CellCycleScoring` function in Seurat (v.5.1.0) was used to score cells according to their cell cycle phase (G1, G2M or S). To define cycling and non-cycling cells, we recalculated the cell cycle score on the basis of cell cycle markers (`cc.genes.updated.2019`) using the `AddModuleScore` function in Seurat. The recalculated score was named `cc.score`. On the basis of internal testing, we defined cycling cells as those with `cc.score`, `S.score` or `G2M.score` greater than 0.2, and non-cycling cells as those with all scores less than 0.1.

## Construction of pseudotime trajectories

Pseudotime trajectories were constructed to model cellular differentiation dynamics using two R packages, Monocle3 (v.1.3.7, <https://cole-trapnell-lab.github.io/monocle3>) and Slingshot (v.2.14.0). For Monocle3, the Seurat object was converted into a Monocle3 `cell_data_set` object. Root nodes were selected on the basis of known progenitor cell types identified in the UMAP, and cells were subsequently ordered along the trajectory for assignment of pseudotime values. For Slingshot, clustering results and dimensionality reduction coordinates from the Seurat object were used as input. Lineages were inferred on the basis of Seurat clusters or cell types, and pseudotime values were assigned to cells. The pseudotime from lineage 1 was used for downstream analyses.

## Progenitor and lineage score of malignant cells

The progenitor and lineage score were calculated following the method in ref. 29, using only malignant cells identified by CNV (as described in the Methods). RGC-like or cycling progenitor-like cell types were designated as progenitors to serve as the starting point at the top. Progenitor score was estimated as the expression of the progenitor shared program minus the maximal expression of the two differentiation programs, and differentiated cells were further classified on the basis of average gene expression differences to differentiate between astrocyte- or ependymal-like and neuron-like lineages.

## Reporting summary

Further information on research design is available in the Nature Portfolio Reporting Summary linked to this article.

## Data availability

Data generated for this study are available at the Gene Expression Omnibus (accessions GSE269937, GSE314803, GSE314599 and GSE314911). All other data are available in the manuscript or in Supplementary Figures or Tables 1–5. All data needed to evaluate the conclusions of the paper are present in the paper and Extended Data Figs. 1–10.

## Code availability

The data analysis code used in the study is available at GitHub (<https://github.com/combiozone/PROJ-Multiome-EPN-ZR> and <https://github.com/combiozone/CellTypeEstimate>).

56. Lee, H. K. et al. Daam2-PIP5K is a regulatory pathway for Wnt signaling and therapeutic target for remyelination in the CNS. *Neuron* **85**, 1227–1243 (2015).
57. Wang, C. Y. et al. Daam2 phosphorylation by CK2 $\alpha$  negatively regulates Wnt activity during white matter development and injury. *Proc. Natl Acad. Sci. USA* **120**, e2304112120 (2023).
58. Corces, M. R. et al. An improved ATAC-seq protocol reduces background and enables interrogation of frozen tissues. *Nat. Methods* **14**, 959–962 (2017).
59. Muskovic, W. & Powell, J. E. DropletQC: improved identification of empty droplets and damaged cells in single-cell RNA-seq data. *Genome Biol.* **22**, 329 (2021).

**Acknowledgements** This study was supported by a NCI Cancer Center Support Grant, P30 CA021765, St. Jude Children's Research Hospital Research Collaborative on Transcription Regulation in Pediatric Cancer Grant, St. Jude Children's Research Hospital institutional funds, and Alex's Lemonade Stand Foundation 'A' Award; and by P01CA298963-01, R01NS128184, R01CA280203, R01CA284455, U01CA281823, DOD-IDEA (CA220510) and a DOD-IMPACT (CA220247) award (to S.C.M.). S.C.M. is supported by funding from the National Brain Tumor Society and CERN Foundation. This work was also supported by US National Institutes of Health grants R35-NS132230, R01-NS124093, R01-CA223388 to B.D. and K99CA277576 to Y.X.; National Cancer Institute Cancer Target Discovery and Development grant U01-CA217842 to B.D.; and grants from the Helis Medical Research Foundation (to H.K.L.), the Ependymoma Research Foundation (to J.Q.), the NIH/NINDS (2R01NS110859 and R01NS126287 to H.K.L.), the Human Frontier Science Program (LTO018/2022-L to Y.X.), and the Wallace Endowment established by an anonymous donor and the Petrello family (to H.K.L.). Further support was provided by the NMSS postdoctoral fellowship (FG-2407-43793 to J.Z.), P01CA096832 (S.J.B.) and F31CA265285 (K.M.B.). We acknowledge J. Norrie and the Single Cell Core for training and allowing us to use their Chromium machine, and the Christian Mayer laboratory for their generous donation of TrackerSeq plasmids and for guiding us through the initial optimization experiments. We thank A. Ansari and his team for helping us with the application and analysis of the CSI technology to study ZR, and C. Schuurmans for her generous donation of *Plagl1*-related plasmids and valuable advice. Several other St. Jude core facilities were instrumental

in this work, including the Cell and Tissue Imaging Center (CTIC), the Hartwell Center for Bioinformatics & Biotechnology (funded partially by ALSAC, NCI grant P30 CA021765), Robert Throm and the St. Jude Vector Laboratory Shared Resource (funded partially by ALSAC), the Center for Advanced Genome Engineering (CAGE; funded partially by ALSAC, NCI grant P30 CA021765) and the Department of Developmental Neurobiology Flow Cytometry Lab.

**Author contributions** A.S.K., H.S., K.B., B.D. and S.C.M., were involved in the conception and design of the project. A.S.K., S.I., K.Y., H.-C.C., T.Z., R.D., J.Z., H.L., T.B., R.P., B.H. and N.L. performed experiments. A.S.K., S.I., A.B. and E.E. were involved in mouse care. H.S. performed single-cell sequencing analysis and visualization, designed and created all single-cell figures, and managed single-cell data. H.S., A.S.K., S.V., N.L., K.Y., J.Z., H.L., S.C. and S.C.M. organized figures. S.V. performed bulk sequencing analysis and visualization. N.L. performed CSI experiments and visualization. K.L. performed flow sorting for TrackerSeq experiments. S.M.P.-M., J.P.C. and Y.-D.W. expanded and validated the TrackerSeq library. K.M.B. and S.J.B. provided guidance and assistance on OPC experiments. S.C.M., A.S.K., H.S., N.L., P.C. and S.V. wrote the manuscript, and A.S.K., H.S., S.I., N.L., S.V., K.Y., H.-C.C., E.E., T.Z., R.M.D., J.P.C., Y.-D.W., J.Z., H.L., K.L., T.B., R.P., A.B., S.M., S.C., A.A., B.H., K.M.B., G.K., T.W., E.C., M.P., A.H., D.G., J.M., Y.X., S.K.M., T.E.M., J.Q., A.D.D., L.A.S., L.W., A.M.D., N.K.F., S.A., A.L. S.J.B., D.W.E., H.K.L., S.M.P.-M., K.C.B., B.D. and S.C.M. were involved in editing the manuscript.

**Competing interests** The authors report no competing interests.

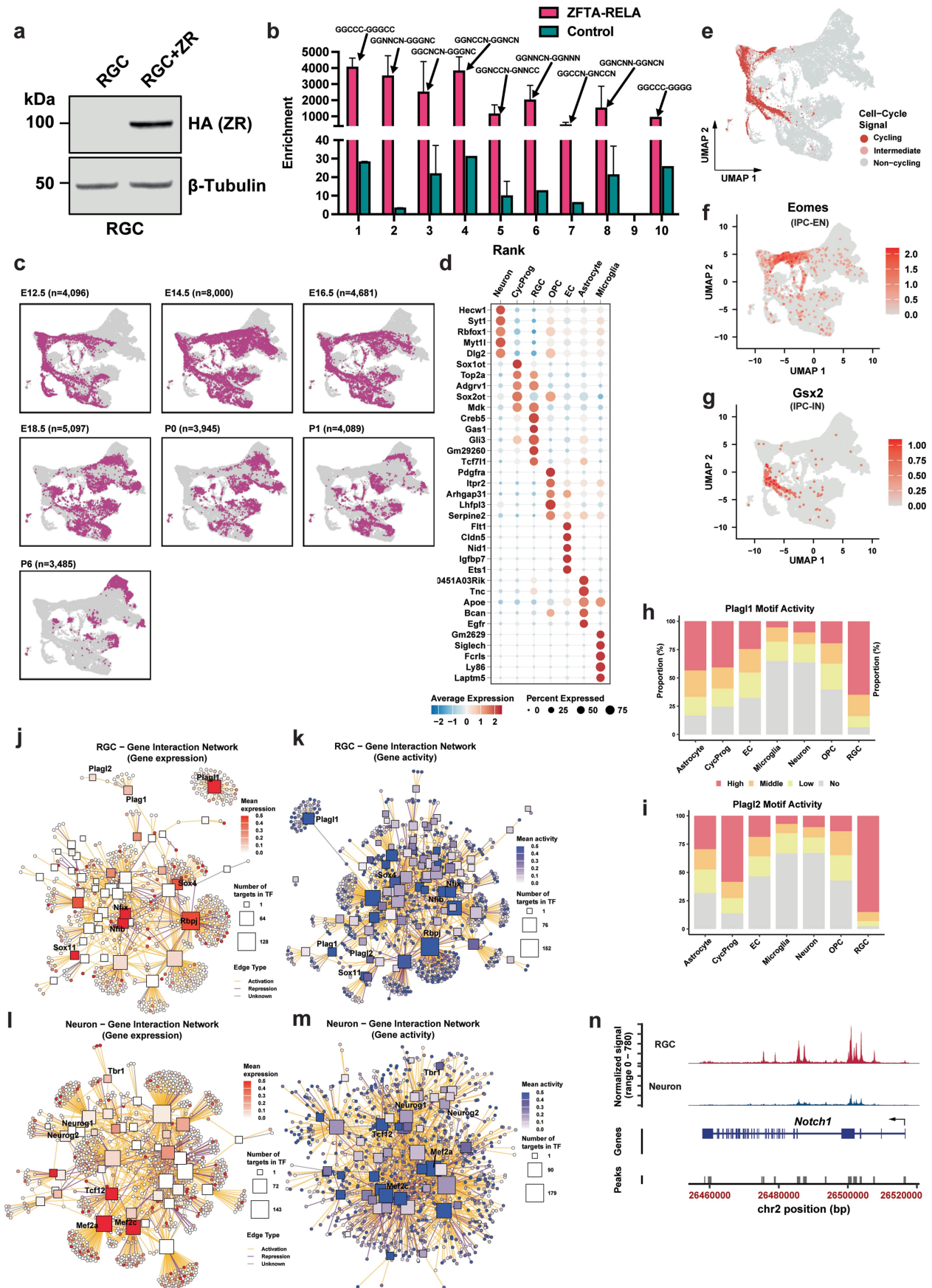
#### **Additional information**

**Supplementary information** The online version contains supplementary material available at <https://doi.org/10.1038/s41586-026-10270-8>.

**Correspondence and requests for materials** should be addressed to Kelsey C. Bertrand, Benjamin Deneen or Stephen C. Mack.

**Peer review information** *Nature* thanks Michelle Monje and the other, anonymous, reviewer(s) for their contribution to the peer review of this work. Peer reviewer reports are available.

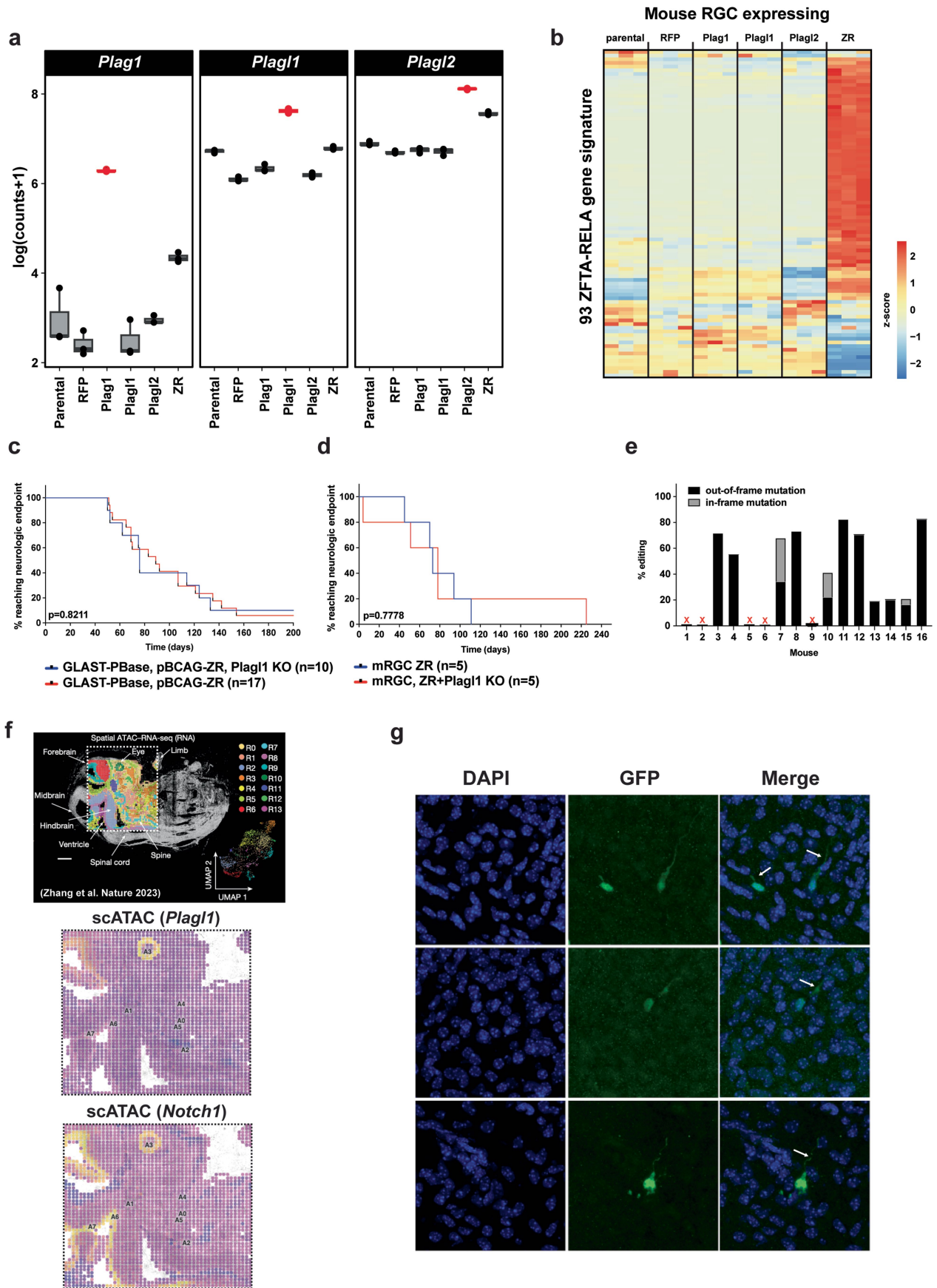
**Reprints and permissions information** is available at <http://www.nature.com/reprints>.



Extended Data Fig. 1 | See next page for caption.

**Extended Data Fig. 1 | Multi-layered analysis of mouse forebrain development: cell distribution, cell type marker expression, transcription factor regulatory networks, and Plagl family motif activity.** (a) Western blot gel image showing expression of HA-tagged ZFTA-RELA (ZR) in RGC + ZR cells compared to control radial glial cells (RGCs).  $\beta$ -Tubulin serves as the loading control. (b) Cognate Site Identification (CSI) experiment to analyze the binding affinity of ZR for PLAG/L family motifs with results ranked by binding motif enrichment. (c) Cell distribution per sample and total cell counts in the integrated UMAP. (d) Top 5 markers for each cell type and corresponding gene expression. (e) Location of cycling cells on mouse forebrain development UMAP. (f) Gene expression of *Eomes*, a TF that dictates intermediate progenitor

cell (IPC) to excitatory neuron (EN) differentiation, in the excitatory neuron cell group. (g) Gene expression of *Gsx2*, a TF that dictates IPC to inhibitory neuron (IN) differentiation, in the IN cell group. (h-i) *Plagl1* and *Plagl2* motif activities classified as high, middle, low, and absent categories for each cell type in development. Y-axis represents the proportion of cells per cell type at each activity level. (j, l) TF-target gene interaction network in RGCs and neurons, based on snRNA-seq gene expression data, respectively. (k, m) TF-target gene interaction network in RGCs and neurons with associated gene activity from single-nucleus ATAC-seq (snATAC) data, respectively. (n) Comparison of snATAC peak signals in the *Notch1* gene region between RGCs and neuron cell types.

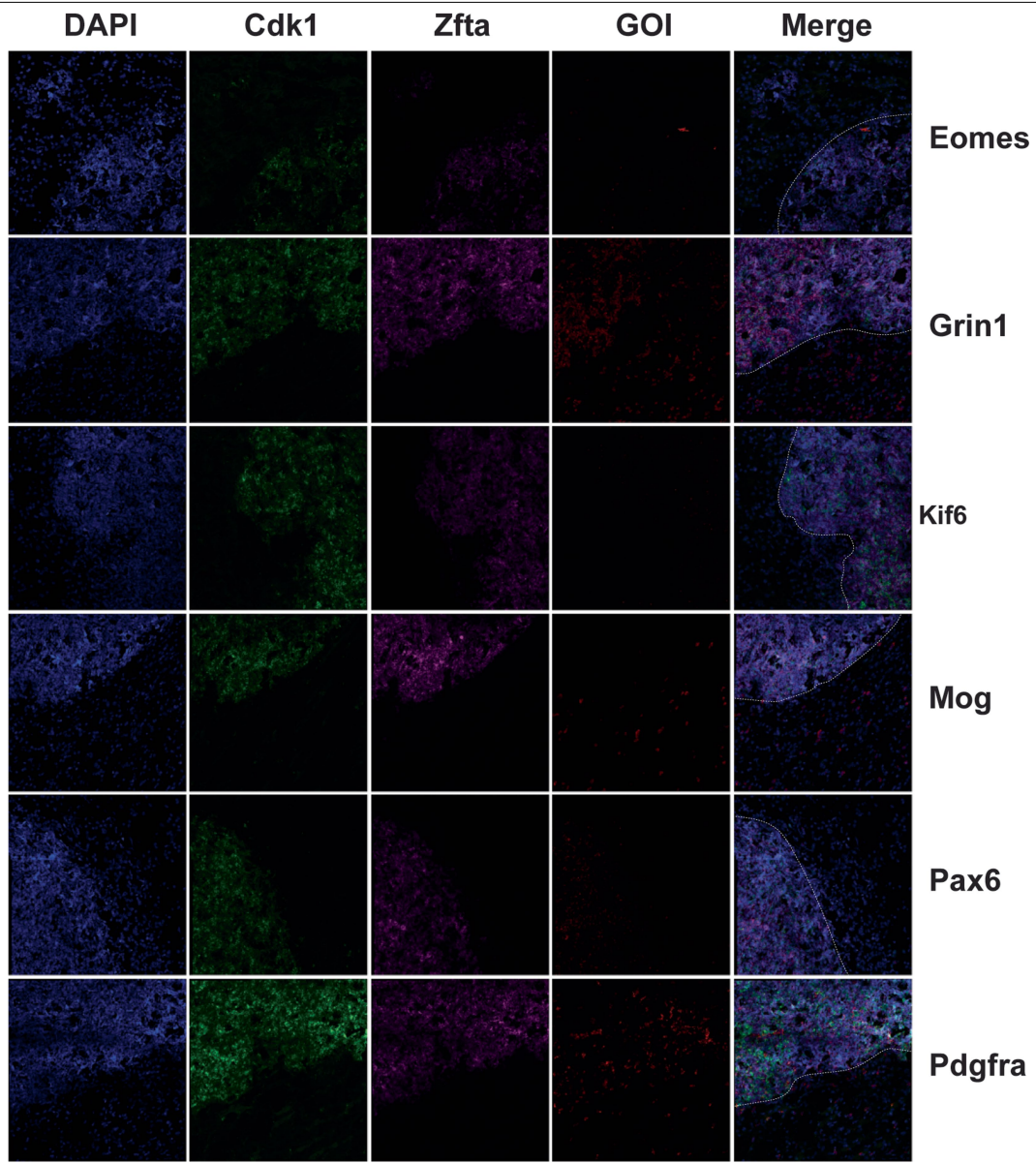


Extended Data Fig. 2 | See next page for caption.

**Extended Data Fig. 2 | Independent studies on gene expression, chromatin accessibility, tissue survival, and immunofluorescence.** (a) Confirmation of *Plag1*, *Plagl1*, and *Plagl2* overexpression in mRGCs by RNA-seq. (b) Heatmap of ZR 93 gene signature for parental, RFP, *Plag1*, *Plagl1*, *Plagl2*, and *ZR* expressing mRGCs by RNA-seq. (c) Survival curve for GLAST-PBase, pBCAG-ZR (red, n = 17) vs GLAST-PBase, pBCAG-ZR, *Plagl1* KO IUE mice (blue, p = 0.8211). (d) Survival curve for mRGC ZR+ (blue, n = 5) vs mRGC ZR+ *Plagl1* KO (red, n = 5) implanted

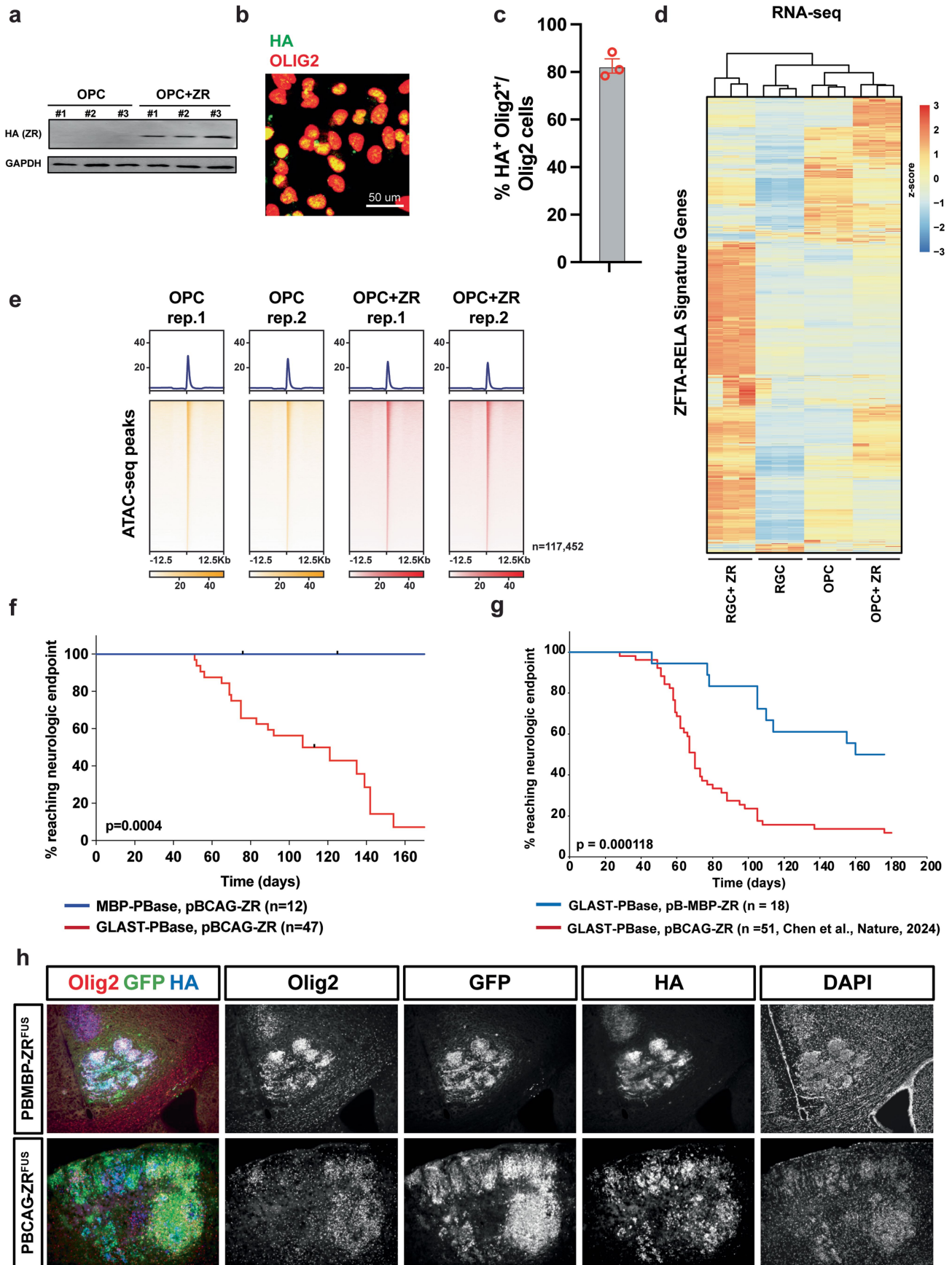
mice (p = 0.7778). (e) Confirmation of *Plagl1* KO for mice within survival curves. Red X denotes a mouse with no knockout which was removed from analysis. (f) Chromatin accessibility signals for *Fabp7*, *Plagl1*, and *Notch1* are detected by spatial scATAC in cells located around the ventricles of mouse embryos. Figure adapted from Zhang et al. Nature 2023. (g) Immunofluorescence for GFP in P2 mice after GFP IUE. Arrows denote radial fibers typical of RGCs.





**Extended Data Fig. 4 | Cell type-specific marker expression in IUEZR tumors detected by RNAscope.** Confirmatory RNAscope of IUEZR tumors for *Cdk1*, *Zfta*, and marker genes for cell types seen in ZR IUE tumors

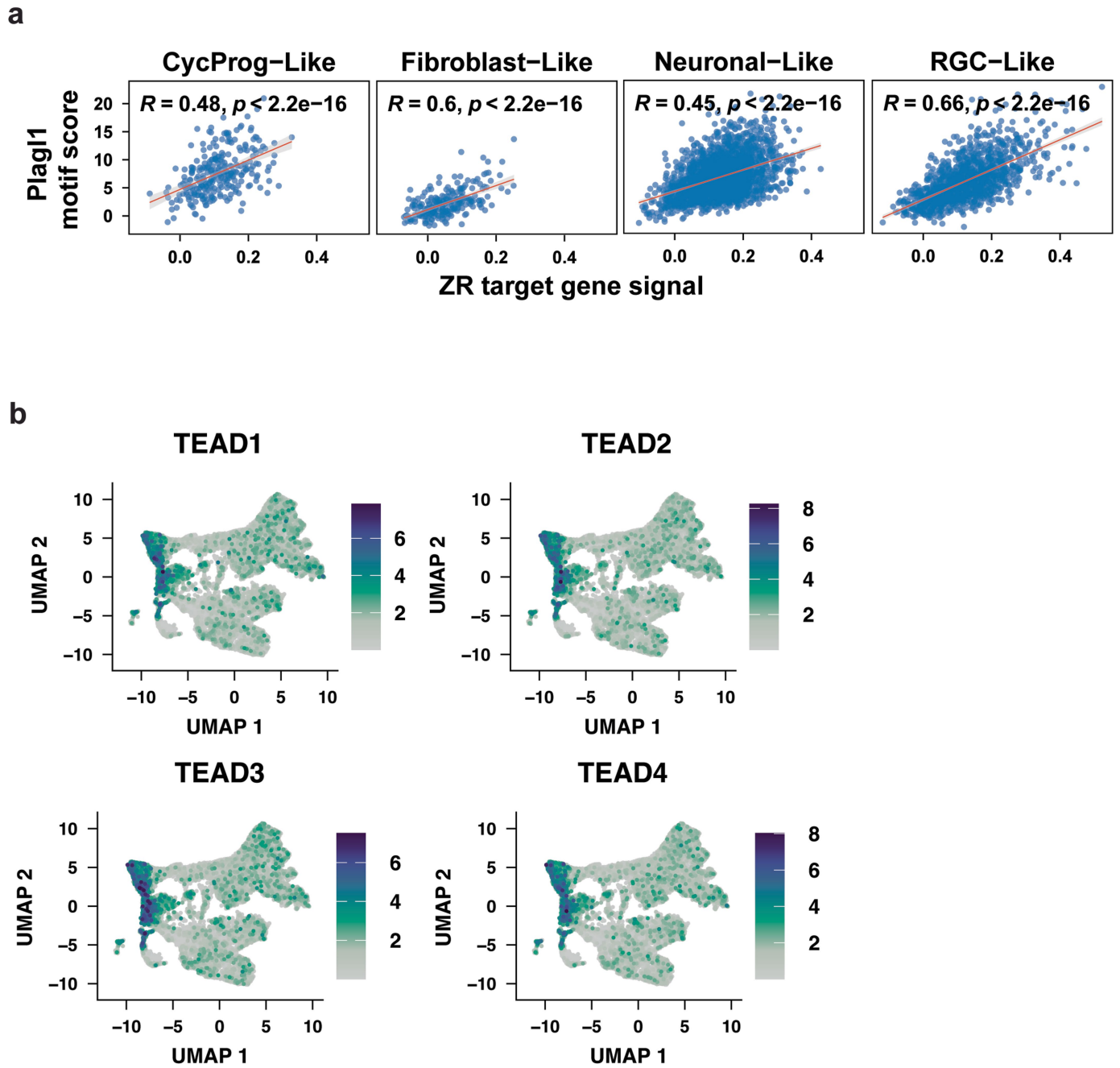
(*Eomes* = early excitatory neurons, *Grin1* = neurons, *Kif6* = ependymal cells, *Mog* = oligodendrocytes, *Pax6* = RGCs, *Pdgfra* = OPCs).



Extended Data Fig. 5 | See next page for caption.

**Extended Data Fig. 5 | Immunofluorescence staining of cell type markers and survival curves of marker-defined cell lines.** (a) Western blot gel image showing expression of HA-tagged ZR in OPC + ZR cells compared to control OPCs. GAPDH serves as the loading control. (b) Immunofluorescent staining of OPCs showing HA (green, tags ZR fusion) and Olig2 (red). (c) Quantification of HA+/Olig2+ cells in immunofluorescent staining. (d) Heatmap of ZR 93 gene expression within RGC, RGC + ZR, OPC, and OPC + ZR cell lines. (e) Global

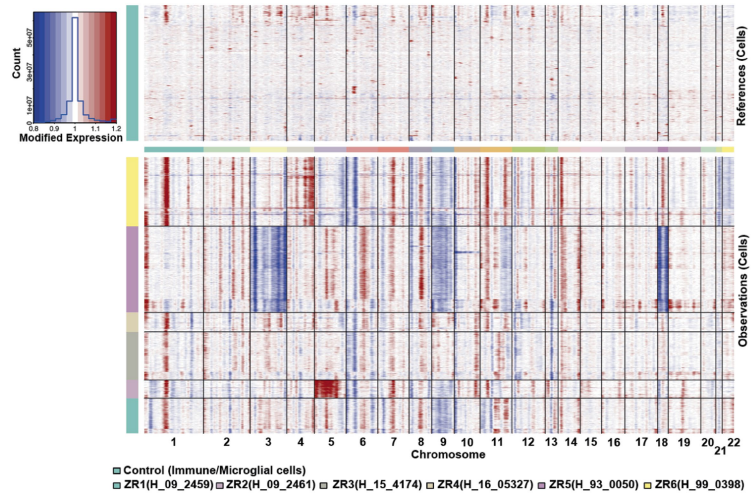
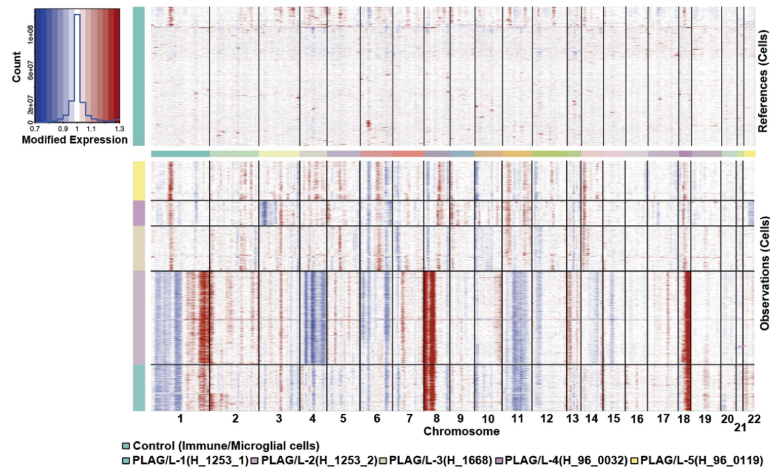
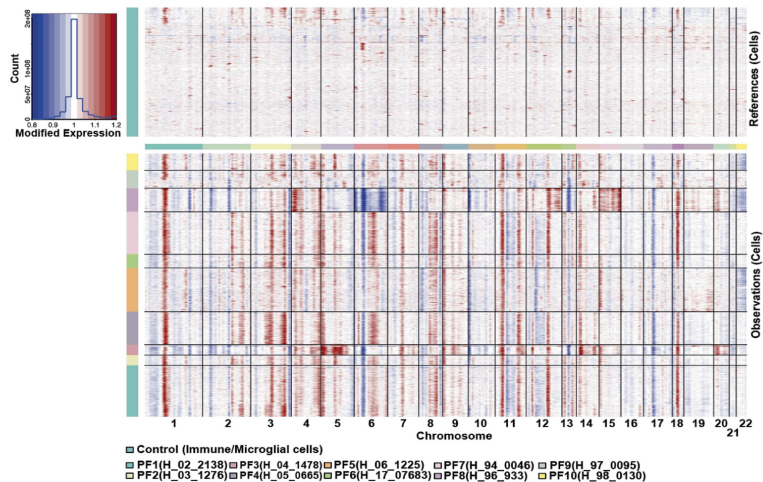
ATAC-seq peak profiles of OPC and OPC + ZR samples, based on two technical replicates. (f) Survival curve for MBP-PBase, pBCAG-ZR (blue, n = 12) GLAST-PBase, pBCAG-ZR (red, n = 47) IUE mice (p = 0.0004). (g) Survival curve for GLAST-PBase, pB-MBP-ZR (blue, n = 18) GLAST-PBase, pBCAG-ZR (red, n = 51, Chen et al. Nature 2024) IUE mice (p = 0.000118). (h) Immunofluorescent staining of GLAST-PBase, pB-MBP-ZR (top row) and GLAST-PBase, pBCAG-ZR (bottom row) tumors.



**Extended Data Fig. 6 | Shared mechanisms of fusion driven tumors.**

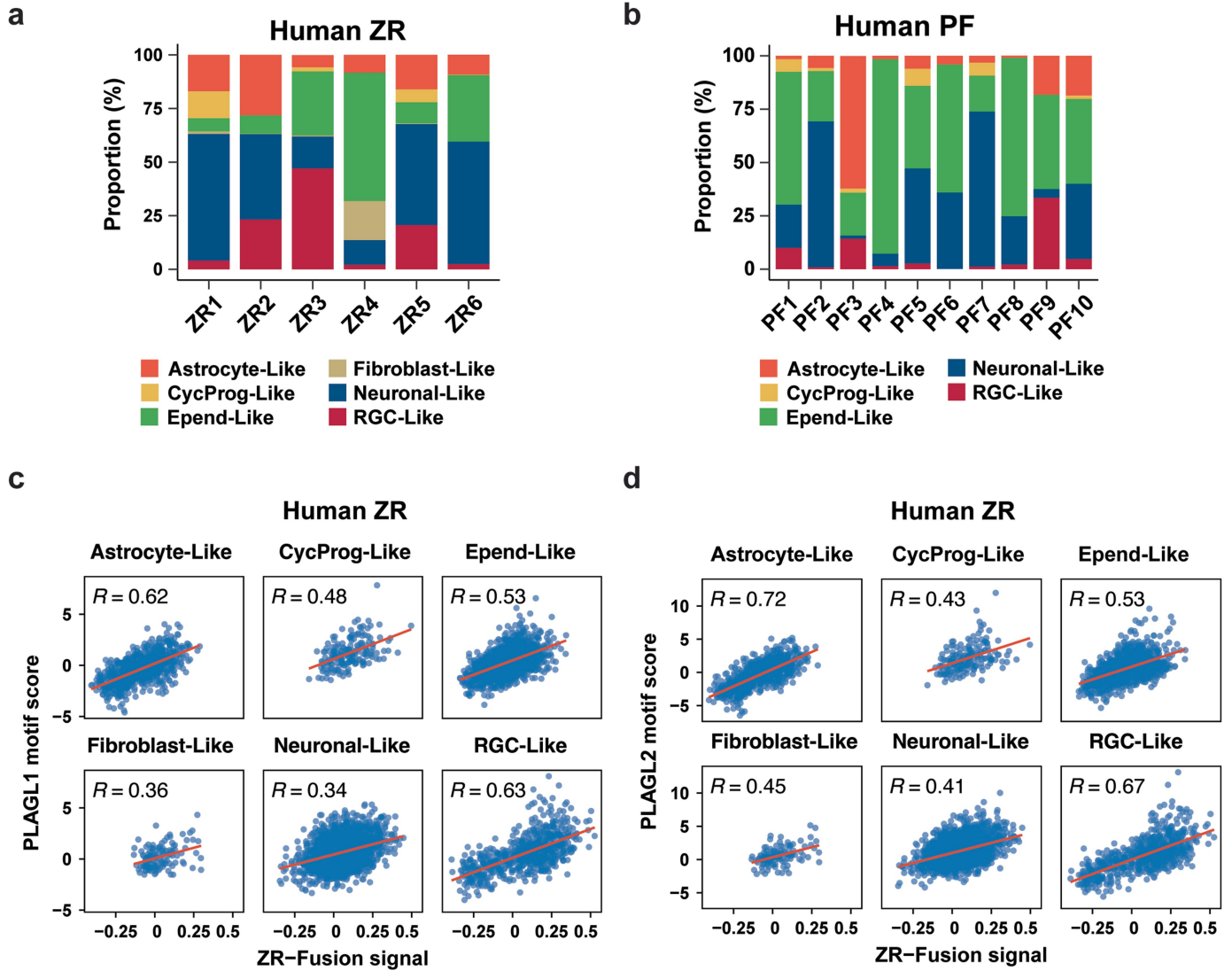
(a) Correlation between *Plagl1* motif score and ZR target gene signal for cycling progenitor-like, fibroblast-like, neuronal-like, and RGC-like IUE ZR tumor cells.

(b) Depiction of Tead1-4 motif activity enriched in RGCs and cycling progenitor cells during embryonic brain development.

**a****Human ZR****b****Human PLAG/L****c****Human PF**

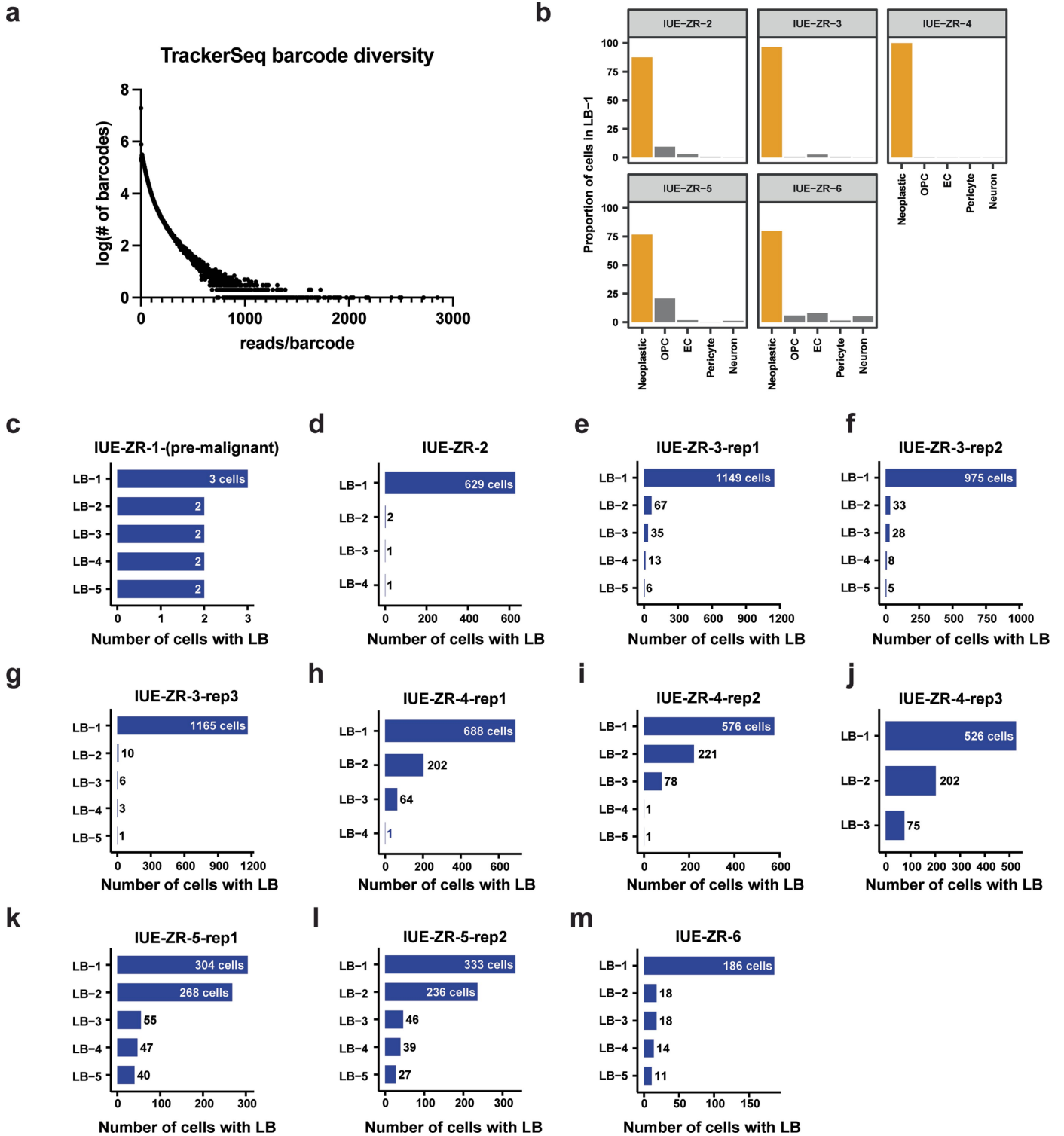
**Extended Data Fig. 7 | Copy number variation landscape of human ZR and PLAG/L brain tumors. (a, b)** Copy number variation (CNV) profiles of human ZR (a), PLAG/L (b), and PF (c) tumors across samples, derived from snRNA-seq

data. The analysis reveals genomic alterations and distinct, sample-specific CNV patterns, particularly within each tumor cohort.



**Extended Data Fig. 8 | Cell type proportion and PLAGL motif-ZR target gene correlation in human ependymomas.** (a, b) Bar plots showing the proportions of cell types per sample in human ZR (a) and PF (b) tumors, highlighting cellular heterogeneity across samples. (c, d) Correlation between

PLAGL1 (c) and PLAGL2 (d) motif activity and ZR target gene signal across distinct cell types in human ZR tumors, including astrocyte-like, cycling progenitor-like, ependymal-like, neuronal-like, and RGC-like cells.

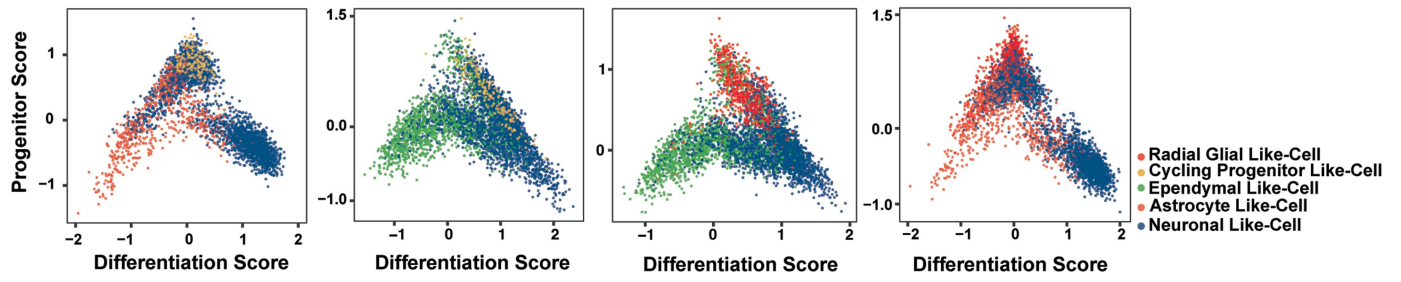


**Extended Data Fig. 9 | Distribution of lineage barcodes and the number of cells per barcode across samples.** (a) TrackerSeq barcode diversity.

(b) Proportion of cells in LB-1 across all neoplastic and non-neoplastic cell types

per sample. (c-m) The bar plot displays the top 5 single lineage barcodes with the highest cell counts per sample.

Human ZR Malignant Tumor Cells



**Extended Data Fig. 10 | Early-stage progenitor tumor cells in ZFTA-RELA tumors display cancer stem cell-like differentiation potential into diverse cell types.** Malignant tumor cell trajectories predicted by progenitor and

differentiation scores demonstrate a transition from progenitor-like cells (RGC-/CycProg-like) to glial-like and neuronal-like cell types in human ZR ependymomas.

## Reporting Summary

Nature Portfolio wishes to improve the reproducibility of the work that we publish. This form provides structure for consistency and transparency in reporting. For further information on Nature Portfolio policies, see our [Editorial Policies](#) and the [Editorial Policy Checklist](#).

### Statistics

For all statistical analyses, confirm that the following items are present in the figure legend, table legend, main text, or Methods section.

n/a Confirmed

- The exact sample size ( $n$ ) for each experimental group/condition, given as a discrete number and unit of measurement
- A statement on whether measurements were taken from distinct samples or whether the same sample was measured repeatedly
- The statistical test(s) used AND whether they are one- or two-sided  
*Only common tests should be described solely by name; describe more complex techniques in the Methods section.*
- A description of all covariates tested
- A description of any assumptions or corrections, such as tests of normality and adjustment for multiple comparisons
- A full description of the statistical parameters including central tendency (e.g. means) or other basic estimates (e.g. regression coefficient) AND variation (e.g. standard deviation) or associated estimates of uncertainty (e.g. confidence intervals)
- For null hypothesis testing, the test statistic (e.g.  $F$ ,  $t$ ,  $r$ ) with confidence intervals, effect sizes, degrees of freedom and  $P$  value noted  
*Give  $P$  values as exact values whenever suitable.*
- For Bayesian analysis, information on the choice of priors and Markov chain Monte Carlo settings
- For hierarchical and complex designs, identification of the appropriate level for tests and full reporting of outcomes
- Estimates of effect sizes (e.g. Cohen's  $d$ , Pearson's  $r$ ), indicating how they were calculated

*Our web collection on [statistics for biologists](#) contains articles on many of the points above.*

### Software and code

Policy information about [availability of computer code](#)

**Data collection** Single cell sequencing data was generated using Illumina NovaSeq 6000 system according to the manufacture's instructions. The public single cell data collected from Gene Expression Omnibus (GEO).

**Data analysis** Data processing and downstream analyses were performed using publicly available, open-source software: Cell Ranger v9.0.0, Cell Ranger ARC v2.0.1, MACS2 v2.2.7, BBDuk v37.9, STARv2.7.0, and FeatureCounts v1.6.3. Subsequent analyses were conducted in R and Python, leveraging widely used packages including Seurat v5.1.0, Signac v1.14.0, SoupX, DoubletFinder v2.0.4, DropletQC, Harmony v1.2.3, InferCNV v1.22.0, DESeq2, Monocle3 v1.3.7, and Slingshot v2.14.0, along with our in-house tool CellTypeEstimate (v0.3.1, [github.com/combiozone/CellTypeEstimate](https://github.com/combiozone/CellTypeEstimate)).

For manuscripts utilizing custom algorithms or software that are central to the research but not yet described in published literature, software must be made available to editors and reviewers. We strongly encourage code deposition in a community repository (e.g. GitHub). See the Nature Portfolio [guidelines for submitting code & software](#) for further information.

## Data

Policy information about [availability of data](#)

All manuscripts must include a [data availability statement](#). This statement should provide the following information, where applicable:

- Accession codes, unique identifiers, or web links for publicly available datasets
- A description of any restrictions on data availability
- For clinical datasets or third party data, please ensure that the statement adheres to our [policy](#)

Previously unpublished mouse 10x Multiome and Tracker-seq data and human 10x Multiome data have been deposited in the Gene Expression Omnibus (GEO) under the accession codes GSE269937, GSE314803, GSE314599, and GSE314911.

## Research involving human participants, their data, or biological material

Policy information about studies with [human participants or human data](#). See also policy information about [sex, gender \(identity/presentation\), and sexual orientation](#) and [race, ethnicity and racism](#).

### Reporting on sex and gender

*Use the terms sex (biological attribute) and gender (shaped by social and cultural circumstances) carefully in order to avoid confusing both terms. Indicate if findings apply to only one sex or gender; describe whether sex and gender were considered in study design; whether sex and/or gender was determined based on self-reporting or assigned and methods used. Provide in the source data disaggregated sex and gender data, where this information has been collected, and if consent has been obtained for sharing of individual-level data; provide overall numbers in this Reporting Summary. Please state if this information has not been collected. Report sex- and gender-based analyses where performed, justify reasons for lack of sex- and gender-based analysis.*

### Reporting on race, ethnicity, or other socially relevant groupings

*Please specify the socially constructed or socially relevant categorization variable(s) used in your manuscript and explain why they were used. Please note that such variables should not be used as proxies for other socially constructed/relevant variables (for example, race or ethnicity should not be used as a proxy for socioeconomic status). Provide clear definitions of the relevant terms used, how they were provided (by the participants/respondents, the researchers, or third parties), and the method(s) used to classify people into the different categories (e.g. self-report, census or administrative data, social media data, etc.) Please provide details about how you controlled for confounding variables in your analyses.*

### Population characteristics

*Describe the covariate-relevant population characteristics of the human research participants (e.g. age, genotypic information, past and current diagnosis and treatment categories). If you filled out the behavioural & social sciences study design questions and have nothing to add here, write "See above."*

### Recruitment

*Describe how participants were recruited. Outline any potential self-selection bias or other biases that may be present and how these are likely to impact results.*

### Ethics oversight

*Identify the organization(s) that approved the study protocol.*

Note that full information on the approval of the study protocol must also be provided in the manuscript.

## Field-specific reporting

Please select the one below that is the best fit for your research. If you are not sure, read the appropriate sections before making your selection.

Life sciences  Behavioural & social sciences  Ecological, evolutionary & environmental sciences

For a reference copy of the document with all sections, see [nature.com/documents/nr-reporting-summary-flat.pdf](https://www.nature.com/documents/nr-reporting-summary-flat.pdf)

## Life sciences study design

All studies must disclose on these points even when the disclosure is negative.

### Sample size

Sample size was defined by sample availability. There was no sample-size calculation performed.

### Data exclusions

No data was excluded from the analysis.

### Replication

Two Tracker-Seq samples were assayed with two to three technical replicates each, and one Tracker-Seq sample was run in three biological replicates. Four ATAC-Seq samples were processed with two technical replicates per experiment. No additional replication was required for other experiments, in accordance with the study design.

### Randomization

The study design did not warrant randomization.

### Blinding

The human brain tumor collections were performed in a blinded manner.

# Reporting for specific materials, systems and methods

We require information from authors about some types of materials, experimental systems and methods used in many studies. Here, indicate whether each material, system or method listed is relevant to your study. If you are not sure if a list item applies to your research, read the appropriate section before selecting a response.

## Materials & experimental systems

- n/a  Involved in the study
- Antibodies
- Eukaryotic cell lines
- Palaeontology and archaeology
- Animals and other organisms
- Clinical data
- Dual use research of concern
- Plants

## Methods

- n/a  Involved in the study
- ChIP-seq
- Flow cytometry
- MRI-based neuroimaging

## Animals and other research organisms

Policy information about [studies involving animals](#); [ARRIVE guidelines](#) recommended for reporting animal research, and [Sex and Gender in Research](#)

### Laboratory animals

*For laboratory animals, report species, strain and age OR state that the study did not involve laboratory animals.*

### Wild animals

*Provide details on animals observed in or captured in the field; report species and age where possible. Describe how animals were caught and transported and what happened to captive animals after the study (if killed, explain why and describe method; if released, say where and when) OR state that the study did not involve wild animals.*

### Reporting on sex

*Indicate if findings apply to only one sex; describe whether sex was considered in study design, methods used for assigning sex. Provide data disaggregated for sex where this information has been collected in the source data as appropriate; provide overall numbers in this Reporting Summary. Please state if this information has not been collected. Report sex-based analyses where performed, justify reasons for lack of sex-based analysis.*

### Field-collected samples

*For laboratory work with field-collected samples, describe all relevant parameters such as housing, maintenance, temperature, photoperiod and end-of-experiment protocol OR state that the study did not involve samples collected from the field.*

### Ethics oversight

*Identify the organization(s) that approved or provided guidance on the study protocol, OR state that no ethical approval or guidance was required and explain why not.*

Note that full information on the approval of the study protocol must also be provided in the manuscript.

## Plants

### Seed stocks

*Report on the source of all seed stocks or other plant material used. If applicable, state the seed stock centre and catalogue number. If plant specimens were collected from the field, describe the collection location, date and sampling procedures.*

### Novel plant genotypes

*Describe the methods by which all novel plant genotypes were produced. This includes those generated by transgenic approaches, gene editing, chemical/radiation-based mutagenesis and hybridization. For transgenic lines, describe the transformation method, the number of independent lines analyzed and the generation upon which experiments were performed. For gene-edited lines, describe the editor used, the endogenous sequence targeted for editing, the targeting guide RNA sequence (if applicable) and how the editor was applied.*

### Authentication

*Describe any authentication procedures for each seed stock used or novel genotype generated. Describe any experiments used to assess the effect of a mutation and, where applicable, how potential secondary effects (e.g. second site T-DNA insertions, mosaicism, off-target gene editing) were examined.*